

# Aerosol-radiation feedback deteriorates the wintertime haze in North China Plain

Jiarui Wu<sup>1,7</sup>, Naifang Bei<sup>2</sup>, Bo Hu<sup>3</sup>, Suixin Liu<sup>1</sup>, Meng Zhou<sup>4</sup>, Qiyuan Wang<sup>1</sup>, Xia Li<sup>1,6</sup>, Lang Liu<sup>1</sup>, Tian Feng<sup>1</sup>, Zirui Liu<sup>3</sup>, Yichen Wang<sup>1</sup>, Junji Cao<sup>1,4</sup>, Xuexi Tie<sup>1</sup>, Jun Wang<sup>5</sup>, Luisa T. Molina<sup>6</sup>, and Guohui Li<sup>1,4\*</sup>

<sup>1</sup>Key Lab of Aerosol Chemistry and Physics, SKLLQG, Institute of Earth Environment, Chinese Academy of Sciences, Xi'an, Shaanxi, 710061, China

<sup>2</sup>School of Human Settlements and Civil Engineering, Xi'an Jiaotong University, Xi'an, Shaanxi, 710049, China

<sup>3</sup>State Key Laboratory of Atmospheric Boundary Layer Physics and Atmospheric Chemistry, Institute of Atmospheric Physics, Chinese Academy of Sciences, Beijing, 100029, China

<sup>4</sup>CAS Center for Excellence in Quaternary Science and Global Change, Xi'an, Shaanxi, 710061, China

<sup>5</sup>Department of Chemical and Biochemical Engineering & Interdisciplinary Graduate Program in Geo-Informatics, University of Iowa, Iowa City, Iowa, IA 52242, USA

<sup>6</sup>Molina Center for Energy and the Environment, La Jolla, California, CA 92037, USA

<sup>7</sup>University of Chinese Academy of Science, Beijing, 100049, China

\*Correspondence to: Guohui Li ([ligh@ieecas.cn](mailto:ligh@ieecas.cn))

**Abstract.** Atmospheric aerosols scatter or absorb a fraction of the incoming solar radiation to cool or warm the atmosphere, decreasing surface temperature and altering atmospheric stability to further affect the dispersion of air pollutants in the planetary boundary layer (PBL). In the present study, simulations during a persistent and heavy haze pollution episode from 05 December 2015 to 04 January 2016 in the North China Plain (NCP) were performed using the WRF-Chem model to comprehensively quantify contributions of aerosol shortwave radiative feedback (ARF) to near-surface (around 15 m above the ground surface) PM<sub>2.5</sub> mass concentrations. The WRF-Chem model generally performs well in simulating the temporal variations and spatial distributions of air pollutants concentrations compared to observations at ambient monitoring sites in the NCP, and the simulated diurnal variations of aerosol species are also consistent with the measurements in Beijing. Additionally, the model simulates well the aerosol radiative properties, the downward shortwave flux, and the PBL height against observations in the NCP. During the episode, ARF deteriorates the haze pollution, increasing the near-surface PM<sub>2.5</sub> concentrations in the NCP by 10.2 μg m<sup>-3</sup> or with a contribution of 7.8% on average. Sensitivity studies have revealed that high loadings of PM<sub>2.5</sub> attenuate the incoming solar radiation reaching the surface to cool the low-level atmosphere, suppressing development of PBL, decreasing the surface wind speed, further hindering the PM<sub>2.5</sub> dispersion and consequently exacerbating the haze pollution in the NCP. Furthermore, when the near-surface PM<sub>2.5</sub> mass concentration increases from around 50 to several hundred μg m<sup>-3</sup>, ARF contributes to the near-surface PM<sub>2.5</sub> by more than 20% during daytime in the NCP, substantially aggravating the heavy haze formation. However, when the near-surface PM<sub>2.5</sub> concentration is less than around 50 μg m<sup>-3</sup>, ARF generally reduces the

42 near-surface  $PM_{2.5}$  concentration due to the consequent perturbation of atmospheric dynamic  
43 fields.

44

45

46

47

48

## 49 1 Introduction

50 Atmospheric aerosols, produced both naturally and anthropogenically, influence the  
51 radiative energy budget of the Earth's atmospheric system in many ways. They scatter or  
52 absorb a fraction of the incoming solar radiation to cool or warm the atmosphere, decreasing  
53 surface temperature and altering atmospheric stability (e.g., Ackerman, 1977; Jacobson, 1998,  
54 2002). Also, they serve as cloud condensation nuclei (CCN) and ice nuclei (IN), thus  
55 modifying cloud optical properties and lifetime (e.g., Zhang et al., 2007; Li et al., 2008;  
56 2009). Among those impacts, the scattering and absorption of solar radiation by aerosols and  
57 the associated feedbacks (hereafter referred to as aerosol-radiation feedback or ARF) not only  
58 constitute one of the main uncertainties in climate prediction (IPCC, 2007), but also  
59 substantially affect the atmospheric chemistry by perturbing the temperature profile and  
60 moistures, winds, and planetary boundary layer (PBL) stability (Boucher et al., 2013).  
61 Particularly, as a short-lived pollutant with uneven distribution and physical and chemical  
62 heterogeneities in the atmosphere, ARF varies by more than a factor of ten with location or  
63 time of emissions (Penner et al., 2010).

64 During wildfire with high loading absorbing aerosols, ARF has been reported to heat the  
65 atmosphere and cool the surface, and thence enhance the PBL stability (e.g., Grell et al., 2011;  
66 Fu et al., 2012; Wong et al., 2012). In addition, numerous studies have been performed to  
67 evaluate impacts of ARF of dust on the regional meteorology and climate (e.g., Perez et al.,  
68 2006; D. Zhang et al., 2009; Santese et al., 2010). Anthropogenic aerosols, dominated by  
69 scattering components, such as organics and sulfate, primarily attenuate the incoming solar  
70 radiation down to the surface, cooling the temperature of the low-level atmosphere to  
71 suppress the development of PBL and hinder the aerosol dispersion in the vertical direction  
72 (e.g., Fast et al., 2006; Vogel et al., 2009; Zhang et al., 2010). In addition, the temperature  
73 profile perturbation caused by ARF also alters cloud formation and development, possibly

74 causing the precipitation delay or decrease (e.g., Zhao et al., 2005; Koch and Del Genio, 2010;  
75 Ding et al., 2013).

76 Rapid industrialization and urbanization in China have significantly elevated the  
77 concentrations of aerosols or fine particulate matters ( $PM_{2.5}$ ), causing frequent occurrence of  
78 haze pollution, particularly during wintertime in North China (e.g., Zhang et al., 2013; Pui et  
79 al., 2014). Guo et al. (2014) have elucidated the haze formation mechanism in China,  
80 highlighting the efficient aerosol nucleation and growth during haze episodes. Moreover,  
81 high loading aerosols during heavy haze episodes induce efficient ARF, encumbering the  
82 PBL development and further deteriorating the haze pollution. It is worth noting that ARF  
83 increases precursors for the aerosol nucleation and growth in the PBL, such as sulfuric and  
84 organic gases, causing efficient aerosol nucleation and growth (Zhang et al., 2004; Guo et al.,  
85 2014). Based on field measurements, recent studies have proposed that the high level of  
86  $PM_{2.5}$  increases the stability of PBL due to ARF and further decrease the PBL height (PBLH),  
87 consequently enhancing  $PM_{2.5}$  concentrations ( $[PM_{2.5}]$ ) (Quan et al., 2013; Petaja et al., 2016;  
88 Yang et al., 2016; Tie et al., 2017; Ding et al., 2017). Online-coupled meteorology and  
89 chemistry models have also been used to verify the impact of ARF on the PBLH and  
90 near-surface  $[PM_{2.5}]$  during haze episodes in Europe, Eastern China and Northern China  
91 (Forkel et al., 2012; Z. Wang et al., 2014; Wang et al., 2015; Zhang et al., 2015; Gao et al.,  
92 2015). However, the ARF impact on near-surface  $[PM_{2.5}]$  varies, depending on the evaluation  
93 time and location (Table 1). For example, the two-way coupled WRF-CMAQ system has  
94 been employed to evaluate the ARF contribution to the haze formation in January 2013 over  
95 the North China Plain (NCP), showing that ARF reduces the PBLH by 100 m and enhances  
96 near-surface  $[PM_{2.5}]$  by up to  $140 \mu g m^{-3}$  in Beijing (J. Wang et al., 2014). Therefore, it is  
97 still imperative to comprehensively quantify the ARF contribution to near-surface  $[PM_{2.5}]$   
98 under various pollution levels to provide the underlying basis for supporting the design and



99 implementation of emission control strategies.

100 In this study, simulations are performed using the Weather Research and Forecasting  
101 model with Chemistry (WRF-Chem) to interpret the relationship between the near-surface  
102 [PM<sub>2.5</sub>] and the PBLH and further quantify the ARF contribution to near-surface [PM<sub>2.5</sub>]  
103 under various pollution levels. The model and methodology are described in Section 2.  
104 Analysis results and discussions are presented in Section 3, and summary and conclusions are  
105 given in Section 4.

## 106 2 Model and methodology

### 107 2.1 WRF-Chem model and configurations

108 The WRF-Chem model (Grell et al., 2005) with modifications by Li et al. (2010, 2011a,  
109 b, 2012) is applied to evaluate effects of ARF on the wintertime haze formation in the NCP.  
110 The model includes a new flexible gas phase chemical module, which can be used with  
111 different chemical mechanisms, such as CBIV, RADM2, and SAPRC. In the study, the  
112 SAPRC99 chemical mechanism is used based on the available emission inventory. For the  
113 aerosol simulations, the CMAQ/models3 aerosol module (AERO5) developed by US EPA  
114 has been incorporated into the model (Binkowski and Roselle, 2003). The wet deposition is  
115 based on the method in the CMAQ module and the dry deposition of chemical species  
116 follows Wesely (1989). The photolysis rates are calculated using the FTUV (fast radiation  
117 transfer model) with the aerosol and cloud effects on photolysis (Li et al., 2005, 2011a).

118 It is worth noting that the most recent extension of ISORROPIA, known as ISORROPIA  
119 II, has incorporated a larger number aerosol species (Ca, Mn, K salts) and is designed to be a  
120 superset of ISORROPIA (Fountoukis et al., 2009). However, the ISORROPIA Version II  
121 uses the exact same routines as ISORROPIA to compute the equilibrium composition, which  
122 produces identical results as ISORROPIA when crustal species are not considered. Therefore,  
123 the inorganic aerosols in this study are predicted using ISORROPIA Version 1.7, calculating

124 the composition and phase state of an ammonium-sulfate-nitrate-water inorganic aerosol in  
125 thermodynamic equilibrium with gas phase precursors (Nenes, 1998). In addition, a  
126 parameterization of sulfate heterogeneous formation involving aerosol liquid water (ALW)  
127 has been developed and implemented into the model, which has successfully reproduced the  
128 observed rapid sulfate formation during haze days (Li et al., 2017a). The sulfate  
129 heterogeneous formation from SO<sub>2</sub> is parameterized as a first order irreversible uptake by  
130 ALW surfaces, with a reactive uptake coefficient of  $0.5 \times 10^{-4}$  assuming that there is enough  
131 alkalinity to maintain the high iron-catalyzed reaction rate.

132 The OA module is based on the VBS approach with aging and detailed information can  
133 be found in Li et al. (2011b). The POA components from traffic-related combustion and  
134 biomass burning are represented by nine surrogate species with saturation concentrations (C\*)  
135 ranging from  $10^{-2}$  to  $10^6 \mu\text{g m}^{-3}$  at room temperature (Shrivastava et al., 2008), and assumed  
136 to be semi-volatile and photochemically reactive (Robinson et al., 2007). The SOA formation  
137 from each anthropogenic or biogenic precursor is calculated using four semi-volatile VOCs  
138 with effective saturation concentrations of 1, 10, 100, and  $1000 \mu\text{g m}^{-3}$  at 298 K. The SOA  
139 formation via the heterogeneous reaction of glyoxal and methylglyoxal is parameterized as a  
140 first-order irreversible uptake by aerosol particles with an uptake coefficient of  $3.7 \times 10^{-3}$   
141 (Liggio et al., 2005; Zhao et al., 2006; Volkamer et al., 2007).

142 A persistent air pollution episode from 05 December 2015 to 04 January 2016 in the  
143 NCP is simulated using the WRF-Chem model. During the study episode, the average hourly  
144 [PM<sub>2.5</sub>] in the NCP are approximately  $127.9 \mu\text{g m}^{-3}$ , within the fourth grade of National  
145 Ambient Air Quality Standards with [PM<sub>2.5</sub>] between  $115$  and  $150 \mu\text{g m}^{-3}$  (moderately  
146 polluted, Feng et al., 2016). The persistent and widespread haze pollution episode with high  
147 [PM<sub>2.5</sub>] in the NCP provides a suitable case for observation analyses and model simulations  
148 to investigate ARF effect on haze pollution. Figure 1a shows the model simulation domain,

149 and detailed model configurations can be found in Table 2.

## 150 2.2 Aerosol radiative module

151 In the present study, Goddard shortwave module developed by Chou and Suarez (1999,  
152 2001) is employed to take into account the ARF effect on the haze formation. The aerosol  
153 radiative module developed by Li et al. (2011b) has been incorporated into the **WRF-Chem**  
154 model to calculate the aerosol optical depth (AOD or  $\tau_a$ ), single scattering albedo (SSA or  
155  $\omega_a$ ), and the asymmetry factor ( $g_a$ ).

156 In the CMAQ aerosol module, aerosols are represented by a three-moment approach  
157 with a lognormal size distribution:

$$158 \quad n(\ln D) = \frac{N}{\sqrt{2\pi} \ln \sigma_g} \exp\left[-\frac{1}{2} \left(\frac{\ln D - \ln D_g}{\ln \sigma_g}\right)^2\right] \quad (1)$$

159 Where  $D$  is the particle diameter,  $N$  is the number distribution of all particles in the  
160 distribution,  $D_g$  is the geometric mean diameter, and  $\sigma_g$  is the geometric standard deviation.

161 To calculate the aerosol optical properties, the aerosol spectrum is first divided into 48 bins  
162 from 0.002 to 2.5  $\mu\text{m}$ , with radius  $r_i$ . The aerosols are classified into four types: (1)  
163 internally mixed sulfate, nitrate, ammonium, hydrophilic organics and black carbon, and  
164 water; (2) hydrophobic organics; (3) hydrophobic black carbon; and (4) other unidentified  
165 aerosols. These four kinds of aerosols are assumed to be mixed externally. For the internally  
166 mixed aerosols, the complex refractive index at a certain wavelength ( $\lambda$ ) is calculated based  
167 on the volume-weighted average of the individual refractive index. Given the particle size  
168 and complex refractive index, the extinction efficiency ( $Q_e$ ),  $\omega_a$  and  $g_a$  are calculated  
169 using the Mie theory at a certain wavelength ( $\lambda$ ). The look-up tables of  $Q_e$ ,  $\omega_a$  and  $g_a$  are  
170 established according to particle sizes and refractive indices to avoid multiple Mie scattering  
171 calculation. The aerosol optical parameters are interpolated linearly from the look-up tables  
172 with the calculated refractive index and particle size in the module.

173 The aerosol optical depth (AOD or  $\tau_a$ ) at a certain wavelength ( $\lambda$ ) in a given

174 atmospheric layer  $k$  is determined by the summation over all types of aerosols and all bins:

$$175 \quad \tau_a(\lambda, k) = \sum_{i=1}^{48} \sum_{j=1}^4 Q_e(\lambda, r_i, j, k) \pi r_i^2 n(r_i, j, k) \Delta Z_k \quad (2)$$

176 where  $n(r_i, j, k)$  is the number concentration of  $j$ -th kind of aerosols in the  $i$ -th bin.  $\Delta Z_k$  is  
 177 the depth of an atmospheric layer. The weighted-mean values of  $\sigma$  and  $g$  are then  
 178 calculated by (d'Almeida et al., 1991):

$$179 \quad \omega_a(\lambda, k) = \frac{\sum_{i=1}^{48} \sum_{j=1}^4 Q_e(\lambda, r_i, j, k) \pi r_i^2 n(r_i, j, k) \omega_a(r_i, j, k) \Delta Z_k}{\sum_{i=1}^{48} \sum_{j=1}^4 Q_e(\lambda, r_i, j, k) \pi r_i^2 n(r_i, j, k) \Delta Z_k} \quad (3)$$

$$180 \quad g_a(\lambda, k) = \frac{\sum_{i=1}^{48} \sum_{j=1}^4 Q_e(\lambda, r_i, j, k) \pi r_i^2 n(r_i, j, k) \omega_a(r_i, j, k) g_a(\lambda, r_i, j, k) \Delta Z_k}{\sum_{i=1}^{48} \sum_{j=1}^4 Q_e(\lambda, r_i, j, k) \pi r_i^2 n(r_i, j, k) \omega_a(r_i, j, k) \Delta Z_k} \quad (4)$$

181 When the wavelength-dependent  $\tau_a$ ,  $\omega_a$ , and  $g_a$  are calculated, they can be used in the  
 182 Goddard shortwave module to evaluate the ARF. Detailed information can be found in Li et  
 183 al. (2011b).

### 184 2.3 Data and statistical methods for comparisons

185 The model performance is validated using the available measurements in the NCP,  
 186 including AOD, SSA, PBLH, downward shortwave flux (SWDOWN), aerosol species, and  
 187 air pollutants. The daily AOD is retrieved from Terra- and Aqua- Moderate Resolution  
 188 Imaging Spectroradiometer (MODIS) level 2 products, with a resolution of  $0.1^\circ \times 0.1^\circ$ . The  
 189 hourly SSA is calculated using the measurement of the turbidity meter at the National Center  
 190 for Nanoscience and Technology (NCNST), Chinese Academy of Sciences ( $116.33^\circ\text{E}$ ,  
 191  $39.99^\circ\text{N}$ ) in Beijing (Figure 1b). The daily PBLH at 12:00 Beijing time (BJT) is diagnosed  
 192 from the radiosonde observation at a meteorological site ( $116.47^\circ\text{E}$ ,  $39.81^\circ\text{N}$ ) in Beijing. The  
 193 SWDOWN is measured by CM-11 pyranometers at four sites from Chinese Ecosystem  
 194 Research Network (CERN) in the NCP (Liu et al., 2016). The hourly measurements of  $\text{O}_3$ ,  
 195  $\text{NO}_2$ ,  $\text{SO}_2$ ,  $\text{CO}$  and  $\text{PM}_{2.5}$  concentrations have been released by the China's Ministry of  
 196 Ecology and Environment (China MEP) since 2013. The hourly submicron sulfate, nitrate,  
 197 ammonium, and organic aerosols are measured by the Aerodyne Aerosol Chemical

198 Speciation Monitor (ACSM) at NCNST. The primary organic aerosol (POA) and SOA  
199 concentrations are obtained from the ACSM measurement analyzed using the Positive Matrix  
200 Factorization (PMF). In addition, we have also analyzed the relationship between  
201 near-surface [PM<sub>2.5</sub>] and the PBLH retrieved from the Lidar measurement at the Institute of  
202 Remote Sensing and Digital Earth (IRSDE), Chinese Academy of Sciences (116.38°E,  
203 40.00°N) in Beijing (Figure 1b).

204 In the present study, the mean bias (*MB*), root mean square error (*RMSE*) and the index  
205 of agreement (*IOA*) are used to assess the performance of WRF-Chem model simulations  
206 against measurements. The detailed description can be found in Supplementary Information  
207 (SI).

208

## 209 3 Results and discussions

### 210 3.1 Model performance

211 We first define the base simulation in which ARF is considered (hereafter referred to as  
212  $f_{base}$ ), and results from  $f_{base}$  are compared to observations in the NCP. Generally, the  
213 model simulates well the horizontal distributions and temporal variations of PM<sub>2.5</sub>, O<sub>3</sub>, NO<sub>2</sub>,  
214 and SO<sub>2</sub> mass concentrations against measurements in the NCP. Additionally, the model also  
215 reasonably well reproduces the temporal profiles of the aerosol species compared to  
216 observations in Beijing. The detailed model validation of air pollutants in the NCP and the  
217 aerosol species in Beijing can be found in SI.

#### 218 3.1.1 Aerosol radiative properties simulations in NCP

219 Aerosol radiative forcing mainly depends on AOD, SSA, and asymmetry parameter (*g*).  
220 The model validations of AOD and SSA are provided in this study to further evaluate the  
221 aerosol radiative effect on the air pollution. The daily AOD at 550 nm, retrieved from Terra-  
222 and Aqua- MODIS level 2 products, is compared with the simulation. Figure 2a shows the

223 scatter plot of the daily retrieved and simulated AOD averaged in the NCP from 05  
224 December 2015 to 04 January 2016. The simulated daily average AOD correlates well with  
225 the observation, with a correlation coefficient of 0.86. Generally, the retrieved and simulated  
226 AOD increases with deterioration of the haze pollution, but the model considerably  
227 underestimates the AOD against the observation. Figure 2b presents the Taylor diagram  
228 (Taylor, 2001) to show the variance, bias and correlation of the simulated and retrieved AOD  
229 from 05 December 2015 to 04 January 2016. There exists a good relationship between the  
230 simulated and retrieved daily AOD during the study episode, with correlation coefficients  
231 generally ranging from 0.5 to 0.9, and standard deviation mostly varying from 0.25 to 1.0.  
232 Figure 3 shows the pattern comparison of the retrieved and simulated AOD averaged during  
233 the simulation period. The model reasonably reproduces the AOD distribution compared to  
234 the observations in the NCP, but considerably underestimates the AOD. The simulated and  
235 retrieved AOD averaged in the NCP during the simulation period is 0.43 and 0.59,  
236 respectively. It is worth noting that the simulated AOD is not only dependent on the column  
237 aerosol content and constituent, but is also significantly influenced by the relative humidity  
238 (RH) controlling the aerosol hygroscopic growth. Additionally, the satellite retrieved AOD is  
239 subject to contamination by existence of clouds, and considering the high occurrence  
240 frequency of clouds during haze days, the retrieved AOD is generally higher than the  
241 simulation (Engstrom and Ekman, 2010; Chand et al., 2012; Grandey et al., 2013).

242       Aerosols are the mixture of absorbing and scattering constituents in the atmosphere.  
243 Their radiative effect of cooling or warming the atmosphere relies on many parameters, and  
244 SSA is one of the most important (Satheesh et al., 2010). Figure 4 depicts the comparison of  
245 the measured and simulated diurnal profiles of SSA at NCNST in Beijing during the episodes.  
246 The model performs reasonably in simulating the daily variation of SSA in Beijing, with an  
247 *IOA* of 0.69 and a *MB* of 0.0, but the overestimation or underestimation is rather large. SSA

248 is the ratio of scattering to extinction, which is highly sensitive to the relative distribution of  
249 scattering and absorbing aerosol constituents in the atmosphere, and the RH determining the  
250 hygroscopic growth of aerosols. Therefore, the uncertainties of the simulated SSA probably  
251 originated from the model biases of aerosol constituents and the RH.

### 252 3.1.2 Downward solar radiation simulations in North China Plain

253 Figure 5 presents the daily profiles of simulated and observed SWDOWN at ground  
254 surfaces in Beijing, Jiaozhouwan, Luancheng, and Yuancheng from 05 December 2015 to 04  
255 January 2016. The WRF-Chem model simulates well the daily variation of SWDOWN,  
256 especially in Jiaozhouwan, Luancheng, and Yucheng, with *IOAs* around 0.90. The model is  
257 subject to overestimating the SWDOWN against measurements, with *MBs* ranging from 6.3  
258 to 86.2 W m<sup>-2</sup>. The SWDOWN reaching the ground surface is very sensitive to the cloud  
259 cover and optical thickness. However, the WRF-Chem model still has difficulties in  
260 accurately predicting the cloud cover and optical thickness, which might constitute one of the  
261 most important reasons for model biases of the SWDOWN. In addition, the horizontal  
262 resolution used in simulations cannot adequately resolve the cumulus clouds, also causing  
263 uncertainties in the simulations of the SWDOWN.

### 264 3.1.3 PBLH simulations in Beijing

265 Figure 6 shows the temporal variations of the observed and simulated PBLH at a  
266 meteorological site in Beijing from 05 December 2015 to 04 January 2016. The average  
267 PBLH at 12:00 BJT during the episode at the meteorological site is 465.2 m, with the  
268 minimum of 101.8 m and the maximum of 1017.9 m, showing decreased PBLH during the  
269 haze episode. In general, the WRF-Chem model tracks reasonably the daily variation of the  
270 PBLH in Beijing, with an *IOA* of 0.70. However, the model has difficulties in reproducing  
271 the observed very low PBLH, e.g., less than 200 m. The PBLH varies substantially with time  
272 due to many factors including large-scale dynamics, cloudiness, convective mixing, and the

273 diurnal cycle of solar radiation (Sivaraman et al., 2013). Therefore, the simulation  
274 uncertainties of meteorological conditions constitute the main reason for the simulation bias  
275 of PBLH. For example, the overestimation of SWDOWN at 12:00 BJT (Figure 5a) probably  
276 caused the overestimation of PBLH in Beijing.

277 In general, the simulated variations of SWDOWN, PBLH, aerosol radiative properties,  
278 air pollutants ( $\text{PM}_{2.5}$ ,  $\text{O}_3$ ,  $\text{NO}_2$ ,  $\text{SO}_2$ ,  $\text{CO}$ ) and aerosol species are in good agreement with  
279 observations, indicating that the simulations of meteorological conditions, chemical processes  
280 and the emission inventory used in the WRF-Chem model are reasonable, providing a  
281 reliable basis for the further investigation.

### 282 3.2 Relationship between near-surface $[\text{PM}_{2.5}]$ and PBLH

283 Figure 7 presents the scatter plot of the Lidar retrieved PBLH at IRSDE and  
284 near-surface  $[\text{PM}_{2.5}]$  at a monitoring site close to IRSDE during daytime (08:00 ~ 17:00 LT)  
285 from 08 January to 20 February 2014. The wind speeds (WSPD) at a meteorological site  
286 close to IRSDE are shown by the color of the filled circles in Figure 7. Additionally,  
287 near-surface  $[\text{PM}_{2.5}]$  during daytime are also subdivided into 20 bins with the interval of 25  
288  $\mu\text{g m}^{-3}$ . The PBLH as the bin of near-surface  $[\text{PM}_{2.5}]$  is assembled, and an average of PBLH  
289 in each bin is calculated (Nakajima et al., 2001; Kawamoto et al., 2006), which is represented  
290 by the rectangle in Figure 7. Generally, on average, when the PBLH decreases from 1500 m  
291 to around 400 m, the near-surface  $[\text{PM}_{2.5}]$  increase from 10 to more than 200  $\mu\text{g m}^{-3}$ . When  
292 near-surface  $[\text{PM}_{2.5}]$  exceed 200  $\mu\text{g m}^{-3}$ , the PBLH remains 400~500 m. Previous studies  
293 have also reported the nonlinear relationship between the PBLH and near-surface  $[\text{PM}_{2.5}]$ ,  
294 and proposed that increasing  $[\text{PM}_{2.5}]$  reduce the PBLH or the ARF is attributed to the PBLH  
295 decrease (e.g., Petaja et al., 2016; Tie et al., 2017; Liu et al., 2018).

296 The PBLH is primarily determined by the wind shear in the vertical direction and the  
297 thermal condition of ground surfaces. The occurrence of low near-surface  $[\text{PM}_{2.5}]$  generally



328 corresponds to efficient dispersions of PM<sub>2.5</sub> in horizontal and/or vertical directions. The  
329 strong horizontal winds in the lower atmosphere not only disperse PM<sub>2.5</sub> emitted or formed  
330 efficiently, but also intensify the wind shear in the vertical direction, increasing the PBLH  
331 and facilitating the rapid vertical exchange of PM<sub>2.5</sub> in the PBL. When near-surface [PM<sub>2.5</sub>]  
332 are less than 50 μg m<sup>-3</sup>, the PBLH exceeding 1000 m is observed, which is chiefly  
333 determined by strong horizontal winds and less influenced by the ground thermal condition  
334 during wintertime, and the observed average WSPD is about 2.4 m s<sup>-1</sup>. The occurrence of  
335 high near-surface [PM<sub>2.5</sub>] indicates that the lower atmosphere is stable or stagnant, with weak  
336 horizontal winds and inactive convections, hindering the dispersion of PM<sub>2.5</sub> in the horizontal  
337 and vertical directions. Additionally, as the horizontal winds become weak or calm, the wind  
338 shear in the vertical direction is diminished and the PBLH is dominated by the ground  
339 thermal condition. When near-surface [PM<sub>2.5</sub>] increase from 50 to around 200 μg m<sup>-3</sup>, the  
340 PBLH decreases from around 700 to 400 m, and the average WSPD decreases to 1.8 m s<sup>-1</sup>.  
341 However, the increased PM<sub>2.5</sub> reducing PBLH still cannot be fully attributed to ARF, which  
342 is more likely caused by the decrease of winds or the formation of stagnant situations in the  
343 low-level atmosphere. When near-surface [PM<sub>2.5</sub>] exceed 200 μg m<sup>-3</sup>, the observed PBLH  
344 fluctuates between 400 and 500 m with the average WSPD of around 1.0 m s<sup>-1</sup>, and does not  
345 exhibit continuous decrease with the increasing near-surface [PM<sub>2.5</sub>].

346 Under the stagnant situation with weak winds, the PBLH is more sensitive to the ground  
347 thermal condition. Increasing aerosols or PM<sub>2.5</sub> in the low-level atmosphere attenuate the  
348 SWDOWN to the ground surface and decrease the surface temperature (TSFC) and  
349 turbulence kinetic energy, suppressing the PBL development and further enhancing  
350 near-surface [PM<sub>2.5</sub>]. Therefore, with near-surface [PM<sub>2.5</sub>] exceeding 200 μg m<sup>-3</sup>, the inert  
351 PBLH might be caused by the defect of the Lidar retrieved PBLH. The aerosol backscatter  
352 signal received by Lidar is used to retrieve the PBLH. If the atmosphere is stable, the aerosols

323 near the maximal PBLH are subject to being confined in situ, and the retrieved PBLH is  
324 generally the maximal one. Additionally, it is worth noting that the occurrence of the  
325 wintertime severe haze pollution in the NCP is often accompanied with the high-level  
326 convergence between 500 and 700 hPa, producing a persistent and strong sinking motion in  
327 the mid-lower troposphere to reduce the PBLH and facilitate accumulation of air pollutants  
328 (Wu et al. 2017; Ding et al., 2017). Therefore, a subsidence inversion appears in the lower  
329 layer as a result of the air masses sinking in the middle-troposphere, restraining the PBL  
330 development and determining the maximal PBLH. Hence, it is imperative to evaluate the  
331 contribution of ARF to the PBLH and near-surface [PM<sub>2.5</sub>].

### 332 3.3 Sensitivity studies

333 The conceptual model about the ARF contribution to the heavy haze formation has been  
334 established in previous studies (e.g., Tie et al., 2017; Liu et al., 2018). During wintertime,  
335 under stagnant meteorological situations with weak winds and humid air, air pollutants are  
336 subject to accumulation in the PBL, facilitating the formation of PM<sub>2.5</sub>. Increasing PM<sub>2.5</sub> in  
337 the PBL absorbs or scatters the incoming solar radiation to decrease the TSFC and facilitate  
338 anomalous temperature inversion, subsequently suppressing the vertical turbulent diffusion  
339 and decreasing the PBLH to further trap more air pollutants and water vapor to increase the  
340 RH in the PBL. Increasing RH enhances aerosol hygroscopic growth and multiphase  
341 reactions and augments the particle size and mass, causing further dimming and decrease of  
342 the TSFC and PBLH. The whole process constitutes a positive feedback induced by the  
343 aerosol radiation effect to enhance near-surface [PM<sub>2.5</sub>], which has been proposed in many  
344 studies (Quan et al., 2013; Petaja et al., 2016; Yang et al., 2016; Tie et al., 2017; Ding et al.,  
345 2017; Liu et al., 2018). The noted positive meteorological condition feedback has also been  
346 considered as the main reason for the near-surface PM<sub>2.5</sub> explosive growth (Zhong et al., 2018;  
347 X. Y. Zhang et al., 2018).

348 To comprehensively evaluate the influence of ARF on near-surface [PM<sub>2.5</sub>] during the  
349 haze episode, a sensitivity study has been conducted, in which ARF is turned off (hereafter  
350 referred as  $f_{rad0}$ ). Therefore, the contribution of ARF to near-surface [PM<sub>2.5</sub>] can be  
351 determined by the difference between  $f_{base}$  and  $f_{rad0}$  ( $f_{base} - f_{rad0}$ ). The most polluted  
352 area in the NCP is first selected to verify the conceptual model of the ARF contribution to the  
353 heavy haze formation, with the average near-surface [PM<sub>2.5</sub>] during the haze episode  
354 exceeding 150  $\mu\text{g m}^{-3}$ . Figure 8 provides the temporal variation of near-surface [PM<sub>2.5</sub>],  
355 SWDOWN, TSFC, PBLH, and RH averaged in the selected area during the episode in  $f_{base}$   
356 and  $f_{rad0}$ . Apparently, ARF considerably decreases the solar radiation reaching the ground  
357 surface and correspondingly lowers the TSFC (Figures 8b and 8c). Subsequently, the PBLH  
358 is decreased and the surface RH is increased due to decreasing TSFC during daytime (Figures  
359 8d and 8e). However, the variation trend of near-surface [PM<sub>2.5</sub>], PBLH, TSFC and RH due  
360 to ARF is not similar to that proposed in the conceptual model. During the haze development  
361 stage, whether ARF is considered or not, the TSFC and RH exhibit an increasing trend,  
362 showing the air mass originated from the south, and the PBLH does not consistently decrease  
363 with increasing near-surface [PM<sub>2.5</sub>]. Additionally, the ARF contribution to near-surface  
364 [PM<sub>2.5</sub>] is generally marginal during the haze development stage. During the haze maturation  
365 stage, ARF commences to elevate near-surface [PM<sub>2.5</sub>] appreciably. It is worth noting that,  
366 even if ARF is not considered in  $f_{rad0}$ , the heavy haze pollution still occurs during the  
367 episode. For example, from 17 to 20 December 2015, without ARF, near-surface [PM<sub>2.5</sub>] still  
368 continue to increase from around 30 to 300  $\mu\text{g m}^{-3}$ , and fluctuate between 150 to 300  $\mu\text{g m}^{-3}$   
369 until the occurrence of favorable meteorological conditions on 25 December. Hence,  
370 according to the variation trend of near-surface [PM<sub>2.5</sub>] with and without the ARF  
371 contribution, the continuous accumulation of PM<sub>2.5</sub> during the haze episode is not primarily  
372 caused by ARF, but predominantly induced by the stagnant meteorological conditions as well

373 as the massive air pollutants emissions in the NCP. Figure 9 presents the temporal variation  
374 of AOD at 550nm averaged in the selected area during the episode in  $f_{base}$  and  $f_{rad0}$  to  
375 evaluate the impact of ARF on AOD. Apparently, except from 8 to 11 December, the ARF  
376 contribution to AOD is generally marginal, indicating that ARF does not play an important  
377 role in the column-integrated aerosol abundance. Additionally, the considerable AOD  
378 enhancement from 8 to 11 December is more likely caused by the substantial increase in RH  
379 due to ARF, which facilitates aerosol hygroscopic growth to augment particle size and further  
380 increases AOD. It is worth noting that the extinction of haze aerosols in the PBL also  
381 decreases the photolysis to suppress the photochemistry, further hindering the secondary  
382 aerosol formation to offset effects of ARF on near-surface  $[PM_{2.5}]$ .

383 In order to quantitatively evaluate effects of ARF on near-surface  $[PM_{2.5}]$ , which cannot  
384 be reflected by the temporal variation of near-surface  $[PM_{2.5}]$ , TSFC, PBLH and RH, an  
385 ensemble method is used in this study. The daytime near-surface  $[PM_{2.5}]$  in the NCP during  
386 the episode in  $f_{base}$  are first subdivided into 30 bins with an interval of  $20 \mu\text{g m}^{-3}$ . The  
387 SWDOWN, TSFC, PBLH, the near-surface WSPD, RH, and  $[PM_{2.5}]$  in  $f_{base}$  and  $f_{rad0}$  in  
388 the same grid cell are assembled as the bin  $[PM_{2.5}]$ , respectively, and an average of these  
389 variables in each bin is calculated. Figure 10 shows the decrease of SWDOWN (%), TSFC  
390 ( $^{\circ}\text{C}$ ), PBLH (%), WSPD ( $\text{m s}^{-2}$ ), and the increase of RH (%), not percentage change) and  
391 near-surface  $[PM_{2.5}]$  contribution (%) caused by ARF as a function of bin  $[PM_{2.5}]$ . The  
392 SWDOWN reaching the ground surface almost decreases linearly with the enhancement of  
393 near-surface  $[PM_{2.5}]$ . When ARF is considered, aerosols in the atmosphere absorb or scatter  
394 the incoming solar radiation, directly attenuating the radiation reaching the ground surface.  
395 When near-surface  $[PM_{2.5}]$  exceed  $200 \mu\text{g m}^{-3}$ , the SWDOWN at ground surfaces decreases  
396 by more than 20% (Figure 10a). Moreover, the decrease of the SWDOWN correspondingly  
397 lowers the TSFC and the decrease of the TSFC is generally proportional to near-surface

398 [PM<sub>2.5</sub>], about 0.35 °C per 100 μg m<sup>-3</sup> PM<sub>2.5</sub> (Figure 10b). Interestingly, ARF also decreases  
399 near-surface WSPD by about 0.1~0.2 m s<sup>-1</sup> with near-surface [PM<sub>2.5</sub>] exceeding 80 μg m<sup>-3</sup>  
400 (Figure 10c). When severe air pollution occurs in the NCP during wintertime, atmospheric  
401 convergence occurs in the PBL (Liao et al., 2015; Ding et al., 2017). However, the ARF  
402 induced cooling in the low-level air generates a divergence in NCP, causing the decrease of  
403 near-surface WSPD.

404 The PBLH is primarily determined by the atmospheric dynamic and thermal condition of  
405 ground surfaces. Therefore, the decrease of WSPD and TSFC due to ARF subsequently  
406 suppresses the PBL development and diminishes the PBLH (Figure 10d). When near-surface  
407 [PM<sub>2.5</sub>] are less than 250 μg m<sup>-3</sup>, the PBLH decreases rapidly with increasing [PM<sub>2.5</sub>]. When  
408 the near-surface [PM<sub>2.5</sub>] are between 250 μg m<sup>-3</sup> and 350 μg m<sup>-3</sup>, the decrease of PBLH is  
409 around 28%. With near-surface [PM<sub>2.5</sub>] more than 350 μg m<sup>-3</sup>, the decrease of PBLH exceeds  
410 30%. As for ARF effect on water vapor in the PBL, the conceptual model has proposed that  
411 the decreased PBL induced by ARF weakens the vertical exchange of water vapor or the  
412 dispersion of water vapor is constrained by the shallow PBL (Tie et al., 2017; Liu et al.,  
413 2018). However, Figure 11a shows that ARF decreases the near-surface water vapor content  
414 slightly, by more than 0.1 g kg<sup>-1</sup> with near-surface [PM<sub>2.5</sub>] exceeding 100 μg m<sup>-3</sup>. During the  
415 haze episode in the NCP, the abundant moisture in the PBL is mainly transported from the  
416 south. The divergence due to cooling caused by ARF weakens the prevailing southerly wind  
417 and decreases the moisture transport from the south, reducing the water vapor content in the  
418 NCP. Considering that the RH is sensitive to the temperature with a constant water vapor  
419 content, the ARF induced cooling still increases the near-surface RH (Figure 10e). When  
420 near-surface [PM<sub>2.5</sub>] exceed 300 μg m<sup>-3</sup>, the RH is increased by more than 5%, so the heavy  
421 haze generally causes the air to be more humid.

422 More PM<sub>2.5</sub> emitted or formed are trapped by a shallow PBL caused by ARF, and

423 increased RH promotes the aerosol hygroscopic growth and further multiphase reactions,  
424 progressively enhancing near-surface  $[PM_{2.5}]$  (Figure 10f). When near-surface  $[PM_{2.5}]$  are  
425 more than  $50 \mu\text{g m}^{-3}$ , the contribution of ARF to near-surface  $[PM_{2.5}]$  consistently increases  
426 with the haze deterioration. When the severe haze occurs, i.e., near-surface  $[PM_{2.5}]$  exceed  
427  $250 \mu\text{g m}^{-3}$ , more than 12% or  $30 \mu\text{g m}^{-3}$   $PM_{2.5}$  is contributed by ARF. The simulated ARF  
428 effects on near-surface  $[PM_{2.5}]$  are generally comparable to those reported by previous  
429 studies. Z. Wang et al. (2014) have shown that ARF increases the monthly  $PM_{2.5}$   
430 concentration by 10%-30% in Beijing-Tianjin-Hebei in January 2013. Using the WRF-Chem  
431 model, Gao et al. (2015) have indicated that ARF increases the  $PM_{2.5}$  concentration by 10-50  
432  $\mu\text{g m}^{-3}$  (2%-30%) over Beijing, Tianjin, and south Hebei from 10 to 15 January 2013, a  
433 period with the simulated maximum hourly surface  $PM_{2.5}$  concentration of more than  $600 \mu\text{g}$   
434  $\text{m}^{-3}$ . X. Zhang et al. (2018) have also quantified the aerosol-meteorology interaction effect on  
435  $PM_{2.5}$  concentrations in China in 2014 using the WRF-Chem model, showing that the  
436 increase of  $PM_{2.5}$  concentrations associated with ARF is up to 16% in China. Other previous  
437 studies have also confirmed ARF effect during the heavy haze pollution episode (Wang et al.,  
438 2015; Zhang et al., 2015; Gao et al., 2016). However, when near-surface  $[PM_{2.5}]$  are less than  
439  $50 \mu\text{g m}^{-3}$ , the contribution of ARF to near-surface  $[PM_{2.5}]$  is negative, although ARF  
440 decreases PBLH and increases RH. One of the possible reasons for the negative contribution  
441 of ARF is perturbations of wind fields caused by the ARF induced cooling. Figure 11b  
442 presents the average vertical velocity (the net velocity by combining updrafts and downdrafts)  
443 below about 400 m in  $f_{rad0}$  as a function of near-surface  $[PM_{2.5}]$ . Apparently, when ARF  
444 is not considered, the area with near-surface  $[PM_{2.5}]$  less than  $100 \mu\text{g m}^{-3}$  is generally  
445 controlled by downward airflow, and vice versa for the area with near-surface  $[PM_{2.5}]$  more  
446 than  $100 \mu\text{g m}^{-3}$ . The ARF induced cooling generally cause a downward motion in the PBL  
447 (Figure 11c), which suppresses the upward motion in the area with near-surface  $[PM_{2.5}]$  more

448 than  $100 \mu\text{g m}^{-3}$  to enhance near-surface  $[\text{PM}_{2.5}]$ , but accelerates the downward motion in the  
449 area with near-surface  $[\text{PM}_{2.5}]$  less than  $100 \mu\text{g m}^{-3}$  to strengthen the divergence intensity,  
450 further decreasing near-surface  $[\text{PM}_{2.5}]$ . Countered by the decrease of PBLH and increase of  
451 RH, the ARF contribution becomes positive with near-surface  $[\text{PM}_{2.5}]$  exceeding  $50 \mu\text{g m}^{-3}$ .

452 Figure 12 presents spatial distributions of the average near-surface  $\text{PM}_{2.5}$  contribution  
453 due to ARF during the episode. The average near-surface  $\text{PM}_{2.5}$  contribution caused by ARF  
454 in the NCP is  $10.2 \mu\text{g m}^{-3}$  or 7.8%, with the maximum exceeding  $40 \mu\text{g m}^{-3}$  in the south of  
455 Hebei. On average, the ARF contribution to near-surface  $[\text{PM}_{2.5}]$  is the most significant in  
456 Tianjin, about  $17.6 \mu\text{g m}^{-3}$  or 10.3%, followed by Hebei ( $11.6 \mu\text{g m}^{-3}$  or 9.3%), Shandong  
457 ( $11.5 \mu\text{g m}^{-3}$  or 7.3%), Henan ( $11.2 \mu\text{g m}^{-3}$  or 7.7%), Anhui ( $7.7 \mu\text{g m}^{-3}$  or 7.4%), Beijing  
458 ( $7.3 \mu\text{g m}^{-3}$  or 6.9%), and Jiangsu ( $7.0 \mu\text{g m}^{-3}$  or 6.2%). It is noteworthy that the ARF  
459 contribution during the episode in North China is generally positive, but in its surrounding  
460 area the contribution becomes negative. At a large scale, when the air pollution occurs during  
461 wintertime in North China, the vertical motion over the polluted area generally shows an  
462 ascending-descending-ascending distribution from the surface to the middle level of the  
463 troposphere, and wind directions present a structure of convergence-divergence-convergence  
464 accordingly (Liao et al., 2015; Wu et al., 2017; Ding et al., 2017). ARF cools the low-level  
465 atmosphere and induces a downward motion, which suppresses the upward motion in the  
466 convergence area in North China to increase near-surface  $[\text{PM}_{2.5}]$ , but accelerates the  
467 downward motion in the divergence area to decrease  $[\text{PM}_{2.5}]$ .

468 Furthermore, when ARF is considered, near-surface  $[\text{PM}_{2.5}]$  over the East and South  
469 China Sea are also increased, with an enhancement less than  $5 \mu\text{g m}^{-3}$  (about 3% to more than  
470 15%). Considering the low near-surface  $[\text{PM}_{2.5}]$  over sea, the  $[\text{PM}_{2.5}]$  enhancement might be  
471 caused by the  $\text{PM}_{2.5}$  transport from the continent. Figure 13 shows the spatial distribution of  
472 the TSFC and wind field variation caused by ARF averaged during the episode. Apparently,

473 ARF causes a widespread cooling effect in East China, and the cooling is the most significant  
474 in the NCP, with the maximum TSFC decrease exceeding 1.5°C. The cooling effect in the  
475 NCP induces a weak northerly wind, decreasing the prevailing southerly wind during the  
476 haze episode (Figure 13). Additionally, the cooling effect over the continent also intensifies  
477 the temperature contrast between land and sea, producing a secondary circulation to transport  
478 the PM<sub>2.5</sub> from the continent to the East and South China Sea.

479

#### 480 **4 Conclusions**

481 In the study, a persistent haze pollution episode in the NCP from 05 December 2015 to  
482 04 January 2016 is simulated using the WRF-Chem model to verify the ARF contribution to  
483 the haze formation. Generally, the model reproduces well the spatial distributions and  
484 temporal variations of PM<sub>2.5</sub>, O<sub>3</sub>, NO<sub>2</sub>, SO<sub>2</sub>, and CO mass concentrations against observations  
485 in the NCP. The calculated temporal variations of aerosol species are also consistent with the  
486 ACSM measurement in Beijing, particularly with regard to the simulation of sulfate, nitrate,  
487 and ammonium. Moreover, the model simulates reasonably well the variation of SWDOWN,  
488 PBLH, and aerosol radiative properties during the episode, compared to the measurement.

489 Previous studies have established that a positive feedback induced by ARF causes the  
490 heavy haze formation by modulating the PBL and RH. However, model results demonstrate  
491 that during the haze development stage in the NCP, ARF does not dominate accumulation of  
492 near-surface [PM<sub>2.5</sub>], while ARF considerably enhances near-surface [PM<sub>2.5</sub>] during the haze  
493 mature stage.

494 Ensemble analyses of model results show that, during daytime, ARF attenuates  
495 SWDOWN reaching ground surfaces efficiently, and correspondingly the TSFC  
496 progressively decreases with increasing near-surface [PM<sub>2.5</sub>] in the NCP. The ARF induced  
497 cooling generates a divergence in the low-level atmosphere in the NCP, lowering the



498 near-surface WSPD and decreasing the water vapor transport from the south. The decreased  
499 WSPD and TSFC caused by ARF hinder the PBL development and the PBLH decreases  
500 rapidly with increasing near-surface  $[PM_{2.5}]$ . Although the water content in the NCP is  
501 decreased slightly, the RH is still increased due to the ARF induced cooling. A shallow PBL  
502 and more humid air caused by ARF accelerate the  $PM_{2.5}$  accumulation and secondary  
503 pollutant formation, facilitating heavy haze formation. The contribution of ARF to  
504 near-surface  $[PM_{2.5}]$  increases from 12% to 20% when near-surface  $[PM_{2.5}]$  increase from  
505 250 to  $500 \mu\text{g m}^{-3}$ . However, ARF decreases the  $PM_{2.5}$  level with near-surface  $[PM_{2.5}]$  less  
506 than  $50 \mu\text{g m}^{-3}$ .

507 The average near-surface  $PM_{2.5}$  contribution of ARF during the episode in the NCP is  
508  $10.2 \mu\text{g m}^{-3}$  or 7.8%. ARF aggravates the heavy haze formation in North China, but in its  
509 surrounding area ARF slightly mitigates the haze pollution. Generally, there is a structure of  
510 convergence-divergence-convergence over the polluted area of North China from the surface  
511 to the middle level of the troposphere. A downward motion is induced due to the widespread  
512 cooling effect of the low-level atmosphere caused by ARF, impeding the upward motion in  
513 the convergence area in North China to increase near-surface  $[PM_{2.5}]$ , but accelerating the  
514 downward motion in the divergence area to decrease  $[PM_{2.5}]$ .

515 Although the model performs generally well in simulating air pollutants, aerosol species  
516 and radiative properties, SWDOWN, and PBLH, the uncertainties from meteorological fields  
517 and emission inventory still have potentials to influence ARF evaluation. Particularly, further  
518 studies need to be conducted to improve the AOD simulations. In this study, ARF only  
519 considers the aerosol effect on the solar radiation, and the influence of longwave radiation  
520 also needs to be included. It is worth noting that modification of photolysis by aerosol  
521 scattering or absorbing solar radiation ultimately alters the atmospheric oxidizing capacity to  
522 influence the secondary aerosol formation, which potentially offsets ARF effect on the haze

523 pollution. Hence, further studies need to be performed to evaluate the effect of aerosol  
524 photolysis interaction on the haze pollution. In addition, aerosols play an important role in the  
525 cloud process serving as cloud condensation nuclei (CCN) and ice nuclei (IN). Therefore,  
526 aerosol-cloud interactions (aerosol indirect effect) modify temperature and moisture profiles  
527 and further influence precipitation, leading to potential effects on the atmospheric chemistry  
528 (Wang et al., 2011). Future studies should be performed to investigate the feedbacks of the  
529 aerosol indirect effect on the air pollutants.

530

531

532

533 *Author contribution.* Guohui Li, as the contact author, provided the ideas and financial  
534 support, developed the model code, verified the conclusions, and revised the paper. Jiarui Wu  
535 conducted a research, designed the experiments, carried the methodology out, performed the  
536 simulation, processed the data, prepared the data visualization, and prepared the manuscript  
537 with contributions from all authors. Naifang Bei provided the treatment of meteorological  
538 data, analyzed the study data, validated the model performance, and reviewed the manuscript.  
539 Bo Hu provided the observation data used in the study, synthesized the observation, and  
540 reviewed the paper. Suixin Liu, Meng Zhou, Qiyuan Wang, Zirui Liu, and Yichen Wang  
541 provided the data and the primary data process, and reviewed the manuscript. Xia Li, Lang  
542 Liu, and Tian Feng analyzed the initial simulation data, visualized the model results and  
543 reviewed the paper. Junji Cao, Xuexi Tie, Jun Wang provided critical reviews pre-publication  
544 stage. Luisa T. Molina provided a critical preview and financial support, and revised the  
545 manuscript.

546

547

548 *Acknowledgements.* This work is financially supported by the National Key R&D Plan  
549 (Quantitative Relationship and Regulation Principle between Regional Oxidation Capacity of  
550 Atmospheric and Air Quality (2017YFC0210000)) and National Research Program for Key  
551 Issues in Air Pollution Control (DQGG0105). Luisa Molina acknowledges support from US  
552 NSF Award 1560494.

553

554 **Reference**

- 555 Ackerman, T. P.: Model of effect of aerosols on urban climates with particular applications to  
556 Los-Angeles basin, *J. Atmos. Sci.*, 34, 531-547,  
557 10.1175/1520-0469(1977)034<0531:amoteo>2.0.co;2, 1977.
- 558 Binkowski, F. S. and Roselle S. J.: Models-3 Community Multiscale Air Quality (CMAQ)  
559 model aerosol component: 1. Model description, *J. Geophys. Res.*, 108, 4183,  
560 doi:10.1029/2001JD001409, 2003.
- 561 Boucher, O., Randall, D., Artaxo, P., Bretherton, C., Feingold, G., Forster, P., Kerminen, V.  
562 M., Kondo, Y., Liao, H., Lohmann, U., Rasch, P., Satheesh, S. K., Sherwood, S.,  
563 Stevens, B., and Zhang, X. Y. : Clouds and aerosols. In: *Climate Change 2013: The*  
564 *Physical Science Basis. Contribution of Working Group I to the Fifth Assessment*  
565 *Report of the Intergovernmental Panel on Climate Change.* Cambridge University Press,  
566 Cambridge, United Kingdom and New York, NY, USA, 2013.
- 567 Chand, D., Wood, R., Ghan, S. J., Wang, M. H., Ovchinnikov, M., Rasch, P. J., Miller, S.,  
568 Schichtel, B., and Moore, T.: Aerosol optical depth increase in partly cloudy conditions,  
569 *J. Geophys. Res.-Atmos.*, 117, 8, 10.1029/2012jd017894, 2012.
- 570 China MEP (Ministry of Environmental Protection, China): Air Quality Observation  
571 Real-time Release Platform of MEP Data Center, available at:  
572 <http://106.37.208.233:20035/> (last access: 18 October 2018), 2013a.
- 573 China MEP (Ministry of Environmental Protection, China): Online Monitoring and Analysis  
574 Platform of China Air Quality, available at: <http://www.aqistudy.cn/> (last access: 18  
575 October 2018), 2013b.
- 576 Chen, F. and Dudhia, J.: Coupling an advanced land surface-hydrology model with the Penn  
577 State-NCAR MM5 modeling system. Part I: Model implementation and sensitivity, *Mon.*  
578 *Weather Rev.*, 129(4), 569-585, 2001.
- 579 Chou, M.-D. and Suarez, M. J.: A solar radiation parameterization for atmospheric studies,  
580 NASA Tech. Rep. NASA/TM-1999- 10460, 15, 38 pp., 1999.
- 581 Chou, M.-D. and Suarez, M. J.: A thermal infrared radiation parameterization for  
582 atmospheric studies, NASA/TM-2001-104606, 19, 55 pp., 2001.
- 583 d'Almeida, Koepke, G. A., P., and Shettle, E. P.: Atmospheric aerosols: global climatology  
584 and radiative Characteristics, 261 pp., A. Deepak, Hampton, Va., 1991.
- 585 Ding, A. J., Fu, C. B., Yang, X. Q., Sun, J. N., Petaja, T., Kerminen, V. M., Wang, T., Xie,  
586 Y., Herrmann, E., Zheng, L. F., Nie, W., Liu, Q., Wei, X. L., and Kulmala, M.: Intense  
587 atmospheric pollution modifies weather: a case of mixed biomass burning with fossil  
588 fuel combustion pollution in eastern China, *Atmos. Chem. Phys.*, 13, 10545-10554,  
589 10.5194/acp-13-10545-2013, 2013.
- 590 Ding, A. J., Huang, X., Nie, W., Sun, J. N., Kerminen, V. M., Petäjä, T., Su, H., Cheng, Y. F.,  
591 Yang, X. Q., and Wang, M. H.: Enhanced haze pollution by black carbon in megacities  
592 in China, *Geophys. Res. Lett.*, 43, doi:10.1002/2016GL067745, 2016.
- 593 Ding, Y. H., Wu, P., Liu, Y. J., and Song, Y. F.: Environmental and Dynamic Conditions for  
594 the Occurrence of Persistent Haze Events in North China, *Engineering.*, 3, 266-271,  
595 10.1016/j.eng.2017.01.009, 2017.

- 596 Engstrom, A., and Ekman, A. M. L.: Impact of meteorological factors on the correlation  
597 between aerosol optical depth and cloud fraction, *Geophys. Res. Lett.*, 37, 4,  
598 10.1029/2010gl044361, 2010.
- 599 Fast, J. D., Gustafson, W. I., Easter, R. C., Zaveri, R. A., Barnard, J. C., Chapman, E. G.,  
600 Grell, G., and Peckham, S. E.: Evolution of Ozone, Particulates, and Aerosol Direct  
601 Radiative Forcing in the Vicinity of Houston Using a Fully Coupled  
602 Meteorology-Chemistry-Aerosol Model, *J. Geophys. Res.-Atmos.*, 11, D21,  
603 111(D21):D21305, Medium: X, 2006.
- 604 Feng, T., Bei, N., Huang, R.-J., Cao, J., Zhang, Q., Zhou, W., Tie, X., Liu, S., Zhang, T., Su,  
605 X., Lei, W., Molina, L. T., and Li, G.: Summertime ozone formation in Xi'an and  
606 surrounding areas, China, *Atmos. Chem. Phys.*, 16, 4323-4342,  
607 <https://doi.org/10.5194/acp-16-4323-2016>, 2016.
- 608 Forkel, R., Werhahn, J., Hansen, A.B., Mckeen, S., Peckham, S., Grell, G., Suppan, P.: Effect  
609 of aerosol-radiation feedback on regional air quality - A case study with WRF/Chem,  
610 *Atmos. Environ.*, 53, 202-211, 2012.
- 611 Fountoukis, C., Nenes, A., Sullivan, A., Weber, R., VanReken, T., Fischer, M., Matias, E.,  
612 Moya, M. Farmer, D., and Cohen, R.: Thermodynamic characterization of Mexico City  
613 Aerosol during MILAGRO 2006, *Atmos. Chem. Phys.*, 9, 2141–2156, 2009.
- 614 Fu, J. S., Hsu, N. C., Gao, Y., Huang, K., Li, C., Lin, N. H., and Tsay, S. C.: Evaluating the  
615 influences of biomass burning during 2006 BASE-ASIA: a regional chemical transport  
616 modeling, *Atmos. Chem. Phys.*, 12, 3837-3855, 10.5194/acp-12-3837-2012, 2012.
- 617 Gao, M., Carmichael, G. R., Wang, Y., Saide, P. E., Yu, M., Xin, J., Liu, Z., and Wang, Z.:  
618 Modeling study of the 2010 regional haze event in the North China Plain, *Atmos. Chem.*  
619 *Phys.*, 16, 1673-1691, 10.5194/acp-16-1673-2016, 2016.
- 620 Gao, Y., Zhang, M., Liu, Z., Wang, L., Wang, P., Xia, X., and Tao, M.: Modeling the  
621 feedback between aerosol and meteorological variables in the atmospheric boundary  
622 layer during a severe fog-haze event over the North China Plain, *Atmos. Chem. Phys.*,  
623 15, 1093-1130, 2015.
- 624 Guo, S., Hu, M., Zamora, M. L., Peng, J. F., Shang, D. J., Zheng, J., Du, Z. F., Wu, Z., Shao,  
625 M., Zeng, L. M., Molina, M. J., and Zhang, R. Y.: Elucidating severe urban haze  
626 formation in China, *P. Natl. Acad. Sci. USA.*, 111, 17373-17378,  
627 10.1073/pnas.1419604111, 2014.
- 628 Grandey, B. S., Stier, P., and Wagner, T. M.: Investigating relationships between aerosol  
629 optical depth and cloud fraction using satellite, aerosol reanalysis and general circulation  
630 model data, *Atmos. Chem. Phys.*, 13, 3177-3184, 10.5194/acp-13-3177-2013, 2013.
- 631 Grell, G. A. and Devenyi, D.: A generalized approach to parameterizing convection  
632 combining ensemble and data assimilation techniques, *Geophys. Res. Lett.*, 29(14),  
633 doi:10.1029/2002GL015311, 2002.
- 634 Grell, G. A., Peckham, S. E., Schmitz, R., McKeen, S. A., Frost, G., Skamarock, W. C., and  
635 Eder, B.: Fully coupled “online” chemistry within the WRF model, *Atmos. Environ.*, 39,  
636 6957-6975, 10.1016/j.atmosenv.2005.04.027, 2005.
- 637 Grell, G., Freitas, S. R., Stuefer, M., and Fast, J.: Inclusion of biomass burning in  
638 WRF-Chem: impact of wildfires on weather forecasts, *Atmos. Chem. Phys.*, 11,

- 639 5289-5303, 10.5194/acp-11-5289-2011, 2011.
- 640 Guenther, A., Karl, T., Harley, P., Wiedinmyer, C., Palmer, P. I., and Geron, C.: Estimates of  
641 global terrestrial isoprene emissions using MEGAN (Model of Emissions of Gases and  
642 Aerosols from Nature), *Atmos. Chem. Phys.*, 6, 3181-3210,  
643 <https://doi.org/10.5194/acp-6-3181-2006>, 2006.
- 644 Hong, S.-Y. and Lim, J.-O. J.: The WRF Single-Moment 6-Class Microphysics Scheme  
645 (WSM6), *Asia-Pacific J. Atmos. Sci.*, 42, 129-151, 2006.
- 646 Horowitz, L. W., Walters, S., Mauzerall, D. L., Emmons, L. K., Rasch, P. J., Granier, C., Tie,  
647 X. X., Lamarque, J. F., Schultz, M. G., Tyndall, G. S., Orlando, J. J., and Brasseur, G. P.:  
648 A global simulation of tropospheric ozone and related tracers: Description and  
649 evaluation of MOZART, version 2, *J. Geophys. Res.-Atmos.*, 108, 4784,  
650 <https://doi.org/10.1029/2002jd002853>, 2003.
- 651 Intergovernmental Panel on Climate Change (IPCC). The Physical Science Basis of Climate  
652 Change: Changes in Atmospheric Constituents and in Radiative Forcing. Cambridge  
653 University Press, New York, pp. 26-27, 2007.
- 654 Jacobson, M. Z.: Studying the effects of aerosols on vertical photolysis rate coefficient and  
655 temperature profiles over an urban airshed, *J. Geophys. Res.-Atmos.*, 103, 10593-10604,  
656 [10.1029/98jd00287](https://doi.org/10.1029/98jd00287), 1998.
- 657 Jacobson, M. Z.: Analysis of aerosol interactions with numerical techniques for solving  
658 coagulation, nucleation, condensation, dissolution, and reversible chemistry among  
659 multiple size distributions, *J. Geophys. Res.-Atmos.*, 107, 23, [10.1029/2001jd002044](https://doi.org/10.1029/2001jd002044),  
660 2002.
- 661 Janjic', Z. I.: Nonsingular Implementation of the Mellor -Yamada Level 2.5 Scheme in the  
662 NCEP Meso Model, Ncep Office Note, 436, 2002.
- 663 Kawamoto, K., Hayasaka, T., Uno, I., and Ohara, T.: A cor- relative study on the relationship  
664 between modeled anthro- pogenic aerosol concentration and satellite-observed cloud  
665 properties over east Asia, *J. Geophys. Res.-Atmos.*, 111, 7, [doi:10.1029/2005jd006919](https://doi.org/10.1029/2005jd006919),  
666 2006.
- 667 Koch, D., and Del Genio, A. D.: Black carbon semi-direct effects on cloud cover: review and  
668 synthesis, *Atmos. Chem. Phys.*, 10, 7685-7696,  
669 <http://dx.doi.org/10.5194/acp-10-7685-2010>, 2010.
- 670 Liao, X., Sun, Z., Tang, Y., Pu, W., Li, Z., and Lu, B.: Meteorological mechanism for the  
671 formation of a serious pollution case in Beijing in the background of northerly flow at  
672 upper levels, *Environmental Science*, 36, 801-808, 2015. (in Chinese)
- 673 Li, G., Zhang, R., Fan, J., and Tie, X.: Impacts of black carbon aerosol on photolysis and  
674 ozone, *J. Geophys. Res.*, 110, [10.1029/2005jd005898](https://doi.org/10.1029/2005jd005898), 2005.
- 675 Li, G., Wang, Y., and Zhang, R.: Implementation of a two-moment bulk microphysics  
676 scheme to the WRF model to investigate aerosol-cloud interaction, *J. Geophys. Res.*,  
677 113, D15211, [doi:10.1029/2007JD009361](https://doi.org/10.1029/2007JD009361), 2008a.
- 678 Li, G., Wang, Y., Lee, K.-H., Diao, Y., and Zhang, R.: Increased winter precipitation over  
679 the North Pacific from 1984-1994 to 1995-2005 inferred from the Global Precipitation  
680 Climatology Project, *Geophys. Res. Lett.*, 35, L13821, [doi:10.1029/2008GL034668](https://doi.org/10.1029/2008GL034668),

681 2008b.

682 Li, G., Wang, Y., Lee, K.-H., Diao, Y., and Zhang, R.: Impacts of aerosols on the  
683 development and precipitation of a mesoscale squall line, *J. Geophys. Res.*,  
684 doi:10.1029/2008JD011581, 2009.

685 Li, G., Lei, W., Zavala, M., Volkamer, R., Dusanter, S., Stevens, P., and Molina, L. T.:  
686 Impacts of HONO sources on the photochemistry in Mexico City during the  
687 MCMA-2006/MILAGO Campaign, *Atmos. Chem. Phys.*, 10, 6551-6567,  
688 10.5194/acp-10-6551-2010, 2010.

689 Li, G., Bei, N., Tie, X., and Molina, L. T.: Aerosol effects on the photochemistry in Mexico  
690 City during MCMA-2006/MILAGO campaign, *Atmos. Chem. Phys.*, 11, 5169-5182,  
691 10.5194/acp-11-5169-2011, 2011a.

692 Li, G., Zavala, M., Lei, W., Tsimpidi, A. P., Karydis, V. A., Pandis, S. N., Canagaratna, M.  
693 R., and Molina, L. T.: Simulations of organic aerosol concentrations in Mexico City  
694 using the WRF-CHEM model during the MCMA-2006/MILAGRO campaign, *Atmos.*  
695 *Chem. Phys.*, 11, 3789-3809, 10.5194/acp-11-3789-2011, 2011b.

696 Li, G., Lei, W., Bei, N., and Molina, L. T.: Contribution of garbage burning to chloride and  
697 PM<sub>2.5</sub> in Mexico City, *Atmos. Chem. Phys.*, 12, 8751-8761, 10.5194/acp-12-8751-2012,  
698 2012.

699 Li, G., Bei, N., Cao, J., Huang, R., Wu, J., Feng, T., Wang, Y., Liu, S., Zhang, Q., Tie, X.,  
700 and Molina, L. T.: A possible pathway for rapid growth of sulfate during haze days in  
701 China, *Atmos. Chem. Phys.*, 17, 3301-3316, <https://doi.org/10.5194/acp-17-3301-2017>,  
702 2017a.

703 Li, G., Bei, N., Cao, J., Wu, J., Long, X., Feng, T., Dai, W., Liu, S., Zhang, Q., and Tie, X.:  
704 Widespread and persistent ozone pollution in eastern China during the non-winter  
705 season of 2015: observations and source attributions, *Atmos. Chem. Phys.*, 17,  
706 2759-2774, <https://doi.org/10.5194/acp-17-2759-2017>, 2017b.

707 Liggio, J., Li, S. M., and McLaren, R.: Reactive uptake of glyoxal by particulate matter, *J.*  
708 *Geophys. Res.-Atmos.*, 110, doi: 10.1029/2004jd005113, 2005.

709 Liu, Q., Jia, X. C., Quan, J. N., Li, J. Y., Li, X., Wu, Y. X., Chen, D., Wang, Z. F., and Liu, Y.  
710 G.: New positive feedback mechanism between boundary layer meteorology and  
711 secondary aerosol formation during severe haze events, *Sci. Rep.*, 8, 8,  
712 10.1038/s41598-018-24366-3, 2018.

713 Nakajima, T., Higurashi, A., Kawamoto, K., and Penner, J. E.: A possible correlation  
714 between satellite-derived cloud and aerosol microphysical parameters, *Geophys. Res.*  
715 *Let.*, 28, 1171-1174, doi:10.1029/2000gl012186, 2001.

716 Nenes, A., Pandis, S. N., and Pilinis, C.: ISORROPIA: A new thermodynamic equilibrium  
717 model for multiphase multicomponent inorganic aerosols, *Aquat. Geochem.*, 4, 123-152,  
718 doi:10.1023/a:1009604003981, 1998.

719 Penner, J. E., Xu, L., Liou, C., Assamoi, E., Flanner, M. G., Edwards, R., and McConnell,  
720 J.: Atmospheric absorption: Can observations constrain the direct and indirect effect of  
721 organic and BC aerosols on climate, American Geophysical Union, AGU Fall Meeting  
722 Abstract, 2010.

- 723 Perez, C., Nickovic, S., Pejanovic, G., Baldasano, J. M., and Ozsoy, E.: Interactive  
724 dust-radiation modeling: A step to improve weather forecasts, *J. Geophys. Res.-Atmos.*,  
725 111, 17, 10.1029/2005jd006717, 2006.
- 726 Petäjä, T., Järvi, L., Kerminen, V. M., Ding, A. J., Sun, J. N., Nie, W., Kujansuu, J., Virkkula,  
727 A., Yang, X., and Fu, C. B.: Enhanced air pollution via aerosol-boundary layer feedback  
728 in China, *Sci. Rep.*, 6, 18998, 2016.
- 729 Pui, D. Y. H., Chen, S. C., and Zuo, Z. L.: PM<sub>2.5</sub> in China: Measurements, sources, visibility  
730 and health effects, and mitigation, *Particuology.*, 13, 1-26, 10.1016/j.partic.2013.11.001,  
731 2014.
- 732 Quan, J., Gao, Y., Zhang, Q., Tie, X., Cao, J., Han, S., Meng, J., Chen, P., and Zhao, D.:  
733 Evolution of planetary boundary layer under different weather conditions, and its impact  
734 on aerosol concentrations, *Particuology.*, 11, 34-40,  
735 <https://doi.org/10.1016/j.partic.2012.04.005>, 2013.
- 736 Robinson, A. L., Donahue, N. M., Shrivastava, M. K., Weitkamp, E. A., Sage, A. M.,  
737 Grieshop, A. P., Lane, T. E., Pandis, S. N., and Pierce, J. R.: Rethinking organic  
738 aerosols: semivolatile emissions and photochemical aging, *Science*, 315, 1259–1262,  
739 2007.
- 740 Santese, M., Perrone, M. R., Zakey, A. S., and Tomasi, F. D.: Modeling of Saharan dust  
741 outbreaks over the Mediterranean by RegCM3: case studies, *Atmos. Chem. Phys.*, 10,  
742 133-156, <https://doi.org/10.5194/acp-10-133-2010>, 2010.
- 743 Satheesh, S. K., Vinoj, V., and Krishnamoorthy, K.: Assessment of Aerosol Radiative Impact  
744 over Oceanic Regions Adjacent to Indian Subcontinent Using Multisatellite Analysis,  
745 *Adv. Meteorol.*, 13, 10.1155/2010/139186, 2010.
- 746 Shrivastava, M. K., Lane, T. E., Donahue, N. M., Pandis, S. N., and Robinson, A. L.: Effects  
747 of gas particle partitioning and aging of primary emissions on urban and regional  
748 organic aerosol concentrations, *J. Geophys. Res.-Atmos.*, 113, doi:  
749 10.1029/2007jd009735, 2008.
- 750 Sivaraman, C., McFarlane, S., Chapman E.: Planetary boundary layer (PBL) height value  
751 added product (VAP): Radiosonde retrievals [J/OL], U.S. DOE, Office of Science,  
752 Office of Biological and Environment Research, DOE/SC-ARM/TR-132, 2013.  
753 <http://http://www.doc88.com/p-9032320085477.html> (last access: 25 October 2018).
- 754 Taylor, K: Summarizing multiple aspects of model performance in single diagram, *J.*  
755 *Geophys. Res.*, 106, 7183-7192, 2001.
- 756 Tie, X., Huang, R. J., Cao, J., Zhang, Q., Cheng, Y., Su, H., Chang, D., Pöschl, U., Hoffmann,  
757 T., and Dusek, U.: Severe Pollution in China Amplified by Atmospheric Moisture, *Sci.*  
758 *Rep.*, 7, 15760, 2017.
- 759 Vogel, B., Vogel, H., Bäumer, D., Bangert, M., Lundgren, K., Rinke, R., and Stanelle, T.:  
760 The comprehensive model system COSMO-ART-Radiative impact of aerosol on the  
761 state of the atmosphere on the regional scale, *Atmos. Chem. Phys.*, 9, 8661-8680,  
762 <https://doi.org/10.5194/acp-9-8661-2009>, 2009.
- 763 Volkamer, R., Martini, F. S., Molina, L. T., Salcedo, D., Jimenez, J. L., and Molina, M. J.: A  
764 missing sink for gas-phase glyoxal in Mexico City: Formation of secondary organic  
765 aerosol, *Geophys. Res. Lett.*, 34, doi: 10.1029/2007gl030752, 2007.



- 766 Wang, H., Shi, G. Y., Zhang, X. Y., Gong, S. L., Tan, S. C., Chen, B., Che, H. Z., and Li, T.:  
767 Mesoscale modelling study of the interactions between aerosols and PBL meteorology  
768 during a haze episode in China Jing-Jin-Ji and its near surrounding region - Part 2:  
769 Aerosols' radiative feedback effects, *Atmos. Chem. Phys.*, 15, 3277-3287,  
770 10.5194/acp-15-3277-2015, 2015.
- 771 Wang, J., Wang, S., Jiang, J., Ding, A., Zheng, M., Zhao, B., Wong, D. C., Zhou, W., Zheng,  
772 G., and Wang, L.: Impact of aerosol-meteorology interactions on fine particle pollution  
773 during China's severe haze episode in January 2013, *Environ. Res. Lett.*, 9, 094002,  
774 2014.
- 775 Wang, Y., Wan, Q., Meng, W., Liao, F., Tan, H., and Zhang, R.: Long-term impacts of  
776 aerosols on precipitation and lightning over the Pearl River Delta megacity area in China,  
777 *Atmos. Chem. Phys.*, 11, 12421–12436, [https://doi.org/10.5194/acp-11-12421-](https://doi.org/10.5194/acp-11-12421-2011) 2011,  
778 2011.
- 779 Wang, Z. F., Li, J., Wang, Z., Yang, W. Y., Tang, X., Ge, B. Z., Yan, P. Z., Zhu, L. L., Chen,  
780 X. S., Chen, H. S., Wand, W., Li, J. J., Liu, B., Wang, X. Y., Wand, W., Zhao, Y. L., Lu,  
781 N., and Su, D. B.: Modeling study of regional severe hazes over mid-eastern China in  
782 January 2013 and its implications on pollution prevention and control, *Sci. China-Earth*  
783 *Sci.*, 57, 3-13, 10.1007/s11430-013-4793-0, 2014.
- 784 Wesely, M. L.: Parameterization of surface resistances to gaseous dry deposition in  
785 regional-scale numerical models, *Atmos. Environ.*, 23, 1293-1304,  
786 10.1016/0004-6981(89)90153-4, 1989.
- 787 Wong, D. C., Pleim, J., Mathur, R., Binkowski, F., Otte, T., Gilliam, R., Pouliot, G., Xiu, A.,  
788 Young, J. O., and Kang, D.: WRF-CMAQ two-way coupled system with aerosol  
789 feedback: software development and preliminary results, *Geosci. Model. Dev.*, 5,  
790 299-312, 10.5194/gmd-5-299-2012, 2012.
- 791 Wu, P., Ding, Y. H., and Liu, Y. J.: Atmospheric circulation and dynamic mechanism for  
792 persistent haze events in the Beijing-Tianjin-Hebei region, *Adv. Atmos. Sci.*, 34,  
793 429-440, 10.1007/s00376-016-6158-z, 2017.
- 794 Yang, X., Zhao, C., Guo, J., and Wang, Y.: Intensification of aerosol pollution associated  
795 with its feedback with surface solar radiation and winds in Beijing, *J. Geophys.*  
796 *Res.-Atmos.*, 121, 4093-4099, 2016.
- 797 Zhang, B., Wang, Y., and Hao, J.: Simulating aerosol-radiation-cloud feedbacks on  
798 meteorology and air quality over eastern China under severe haze conditions in winter,  
799 *Atmos. Chem. Phys.*, 15, 2387-2404, 10.5194/acp-15-2387-2015, 2015.
- 800 Zhang, D. F., Zakey, A. S., Gao, X. J., Giorgi, F., and Solmon, F.: Simulation of dust aerosol  
801 and its regional feedbacks over East Asia using a regional climate model, *Atmos. Chem.*  
802 *Phys.*, 9, 1095-1110, 10.5194/acp-9-1095-2009, 2009.
- 803 Zhang, Q., Streets, D. G., Carmichael, G. R., He, K. B., Huo, H., Kannari, A., Klimont, Z.,  
804 Park, I. S., Reddy, S., Fu, J. S., Chen, D., Duan, L., Lei, Y., Wang, L. T., and Yao, Z. L.:  
805 Asian emissions in 2006 for the NASA INTEX-B mission, *Atmos. Chem. Phys.*, 9,  
806 5131-5153, <https://doi.org/10.5194/acp-9-5131-2009>, 2009.
- 807 Zhang, R. Y., Li, G. H., Fan, J. W., Wu, D. L., and Molina, M. J.: Intensification of Pacific  
808 storm track linked to Asian pollution, *P. Natl. Acad. Sci. USA.*, 104, 5295-5299,  
809 10.1073/pnas.0700618104, 2007.

810 Zhang, R., Suh, I., Zhao, J., Zhang, D., Fortner, E. C., Tie, X., Molina, L. T., and Molina, M.  
811 J.: Atmospheric new particle formation enhanced by organic acids, *Science*, 304,  
812 1487-1490, 2004.

813 Zhang, R., Jing, J., Tao, J., Hsu, S.-C., Wang, G., Cao, J., Lee, C. S. L., Zhu, L., Chen, Z.,  
814 Zhao, Y., and Shen, Z.: Chemical characterization and source apportionment of PM<sub>2.5</sub> in  
815 Beijing: seasonal perspective, *Atmos. Chem. Phys.*, 13, 7053-7074,  
816 <https://doi.org/10.5194/acp-13-7053-2013>, 2013.

817 Zhang, X., Zhang, Q., Hong, C. P., Zheng, Y. X., Geng, G. N., Tong, D., Zhang, Y. X., and  
818 Zhang, X. Y.: Enhancement of PM<sub>2.5</sub> Concentrations by Aerosol-Meteorology  
819 Interactions Over China, *J. Geophys. Res.-Atmos.*, 123, 1179-1194,  
820 [10.1002/2017jd027524](https://doi.org/10.1002/2017jd027524), 2018a.

821 Zhang, X. Y., Zhong, J. T., Wang, J. Z., Wang, Y. Q., and Liu, Y. J.: The interdecadal  
822 worsening of weather conditions affecting aerosol pollution in the Beijing area in  
823 relation to climate warming, *Atmos. Chem. Phys.*, 18, 5991-5999,  
824 [10.5194/acp-18-5991-2018](https://doi.org/10.5194/acp-18-5991-2018), 2018b.

825 Zhang, Y., Wen, X. Y., and Jang, C. J.: Simulating chemistry-aerosol-cloud-radiation-climate  
826 feedbacks over the continental U.S. using the online-coupled weather research  
827 forecasting model with chemistry (WRF/Chem), *Atmos. Environ.*, 44(29), 3568-3582,  
828 2010.

829 Zhao, J., Levitt, N. P., and Zhang, R.: Heterogeneous chemistry of octanal and 2,  
830 4-hexadienal with sulfuric acid, *Geophys. Res. Lett.*, 32, L09802,  
831 [doi:10.1029/2004GL022200](https://doi.org/10.1029/2004GL022200), 2005.

832 Zhong, J. T., Zhang, X. Y., Dong, Y. S., Wang, Y. Q., Liu, C., Wang, J. Z., Zhang, Y. M.,  
833 and Che, H. C.: Feedback effects of boundary-layer meteorological factors on  
834 cumulative explosive growth of PM<sub>2.5</sub> during winter heavy pollution episodes in Beijing  
835 from 2013 to 2016, *Atmos. Chem. Phys.*, 18, 247-258, [10.5194/acp-18-247-2018](https://doi.org/10.5194/acp-18-247-2018), 2018.

836

837

838

839

840

841 Table 1 Impact of ARF on near-surface [PM<sub>2.5</sub>] in China  
842

| Reference                 | Time   | Location   | Impact on [PM <sub>2.5</sub> ]   |
|---------------------------|--|--|--|
| Z. Wang et al. (2014)     | January 2013   | Beijing-Tianjin-Hebei  | +10~30%  |
| J. Wang et al. (2014)     | January 2013   | North China Plain  | Up to +140 µg m <sup>-3</sup>  |
| Gao et al. (2015)         | 10-15 January 2013   | Beijing, Tianjin, and south Hebei                                    | +10-50 µg m <sup>-3</sup> (2-30%)                                      |
| Wang et al. (2015)        | 7-11 July 2008   | Beijing, Tianjin, Hebei, East Shanxi, West Shandong, and North Henan | +14%   |
| Zhang et al. (2015)       | January 2013   | Henan, Hubei, Guangxi, and Sichuan                                   | Maximum +69.3 µg m <sup>-3</sup>                                       |
| Ding et al. (2016)        | December 2013  | Eastern China and the Sichuan Basin                                  | Up to +100 µg m <sup>-3</sup>  |
| Gao et al. (2016)         | January 2010   | Shijiazhuang   | More than +20 µg m <sup>-3</sup>                                       |
| X. Y. Zhang et al. (2018) | December 2016  | Beijing  | around +84% of [PM <sub>2.5</sub> ] during cumulative explosive growth |
| Liu et al. (2018)         | 15-21 December 2016  | North China Plain  | +56 µg m <sup>-3</sup>   |
| X. Zhang et al. (2018)    | 2014   | China  | over +16% for the daily maximum [PM <sub>2.5</sub> ]                   |
| Zhong et al. (2018)       | January 2013, February 2014, December 2015, and December 2016 to 10 January 2017 | Beijing  | Over +70% of [PM <sub>2.5</sub> ] during cumulative explosive growth   |

843  
844  
845  
846  
847

848 Table 2 WRF-Chem model configurations.

849

|  |  |
|--|--|
| Region   | East Asia  |
| Simulation period                              | 05 December 2015 to 04 January 2016  |
| Domain size                                    | 400 × 400  |
| Domain center                                  | 35°N, 114°E  |
| Horizontal resolution                          | 12 km × 12 km  |
| Vertical resolution                            | 35 vertical levels with a stretched vertical grid with spacing ranging from 30 m near the surface, to 500 m at 2.5 km and 1 km above 14 km |
| Microphysics scheme                            | WSM 6-class graupel scheme (Hong and Lim, 2006)  |
| Cumulus scheme                                 | Grell-Devenyi ensemble scheme (Grell and Devenyi, 2002)  |
| Boundary layer scheme                          | MYJ TKE scheme (Janjić, 2002)  |
| Surface layer scheme                           | MYJ surface scheme (Janjić, 2002)  |
| Land-surface scheme                            | Unified Noah land-surface model (Chen and Dudhia, 2001)  |
| Longwave radiation scheme                      | Goddard longwave scheme (Chou and Suarez, 2001)  |
| Shortwave radiation scheme                     | Goddard shortwave scheme (Chou and Suarez, 1999)   |
| Meteorological boundary and initial conditions | NCEP 1°×1° reanalysis data   |
| Chemical initial and boundary conditions       | MOZART 6-hour output (Horowitz et al., 2003)   |
| Anthropogenic emission inventory               | Developed by Zhang et al. (2009) and Li et al. (2017), 2012 base year, and SAPRC-99 chemical mechanism                                     |
| Biogenic emission inventory                    | Online MEGAN model developed by Guenther et al. (2006)   |

850

851

852

853

854

855

## Figure Captions

856 Figure 1 (a) WRF-Chem simulation domain with topography and (b) Beijing-Tianjin-Hebei  
857 area. In (a), the blue circles represent centers of cities with ambient monitoring sites  
858 in, and the size of blue circles denotes the number of ambient monitoring sites of  
859 cities. In (b), the blue and red filled circles denote the NCNST and IRSDE site,  
860 respectively, the red filled rectangle denotes the meteorological site. The red numbers  
861 denote the CERN sites with the solar radiation measurement. 1: Beijing urban; 2:  
862 Jiaozhouwan; 3: Yucheng; 4: Luancheng.

863 Figure 2 (a) Scatter plot of the MODIS retrieved and simulated daily AOD, (b) Taylor  
864 diagram (Taylor, 2001) to present the variance, bias and correlation of the retrieved  
865 and simulated daily AOD averaged in the NCP from 05 December 2015 to 04 January  
866 2016.

867 Figure 3 Spatial distribution of (a) retrieved and (b) simulated AOD averaged from 05  
868 December 2015 to 04 January 2016 in the NCP.

869 Figure 4 Comparison of measured (black dots) and predicted (red line) diurnal profiles of  
870 SSA in Beijing from 05 December 2015 to 04 January 2016.

871 Figure 5 Comparison of measured (black dots) and predicted (red line) diurnal profiles of the  
872 SWDOWN reaching the ground surface in (a) Beijing, (b) Jiaozhouwan, (c)  
873 Luancheng, and (d) Yucheng from 05 December 2015 to 04 January 2016.

874 Figure 6 Comparison of predicted diurnal profile (red line) of PBLH from 05 December 2015  
875 to 04 January 2016 with observations at 12:00 BJT in Beijing.

876 Figure 7 Scatter plot of the PBLH and near-surface  $[PM_{2.5}]$  at IRSDE site from 12 January to  
877 20 February 2014. The black rectangle shows the bin average of PBLH. The color of  
878 the filled circles denotes the WSPD at the meteorological site close to IRSDE in  
879 Figure 1b.

880 Figure 8 Temporal variations of the average (a) near-surface  $[PM_{2.5}]$ , (b) SWDOWN at the  
881 ground surface, (c) TSFC, (d) PBLH, and (e) RH in the most polluted area in the NCP  
882 with  $[PM_{2.5}]$  of more than  $150 \mu\text{g m}^{-3}$  in  $f_{base}$  (red solid line) and  $f_{rad0}$  (blue solid  
883 line) from 05 December 2015 to 04 January 2016.

884 Figure 9 Temporal variations of the average AOD at 550nm in the most polluted area in the  
885 NCP with  $[PM_{2.5}]$  of more than  $150 \mu\text{g m}^{-3}$  in  $f_{base}$  (red solid line) and  $f_{rad0}$  (blue  
886 solid line) from 05 December 2015 to 04 January 2016.

887 Figure 10 Average (a) percentage decrease of SWDOWN at the ground surface, (b) decrease  
888 of TSFC, (c) decrease of WSPD, (d) percentage decrease of PBLH, (e) increase of RH,  
889 and (f) percentage contribution of near-surface  $[PM_{2.5}]$  caused by ARF, as a function  
890 of the near-surface  $[PM_{2.5}]$  in the NCP during daytime from 05 December 2015 to 04  
891 January 2016.

892 Figure 11 Average decrease of (a) near-surface water vapor content and (c) vertical velocity  
893 below 400 m caused by ARF, and (b) average vertical velocity below 400 m in  $f_{rad0}$   
894 as a function of the near-surface  $[PM_{2.5}]$  in the NCP during daytime from 05  
895 December 2015 to 04 January 2016.

896 Figure 12 Near-surface  $[PM_{2.5}]$  contribution caused by ARF, averaged from 05 December  
897 2015 to 04 January 2016 in NCP.

898 Figure 13 TSFC and wind filed variations caused by ARF, averaged from 05 December 2015  
899 to 04 January 2016 in NCP.

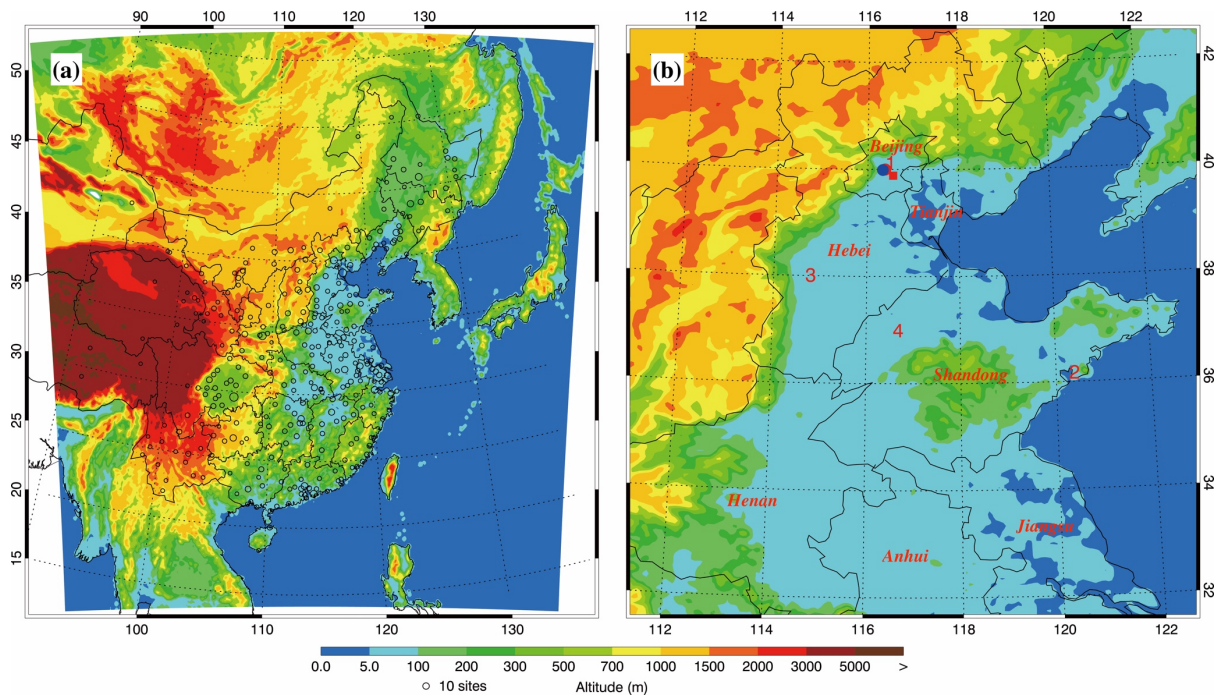
900

901

902

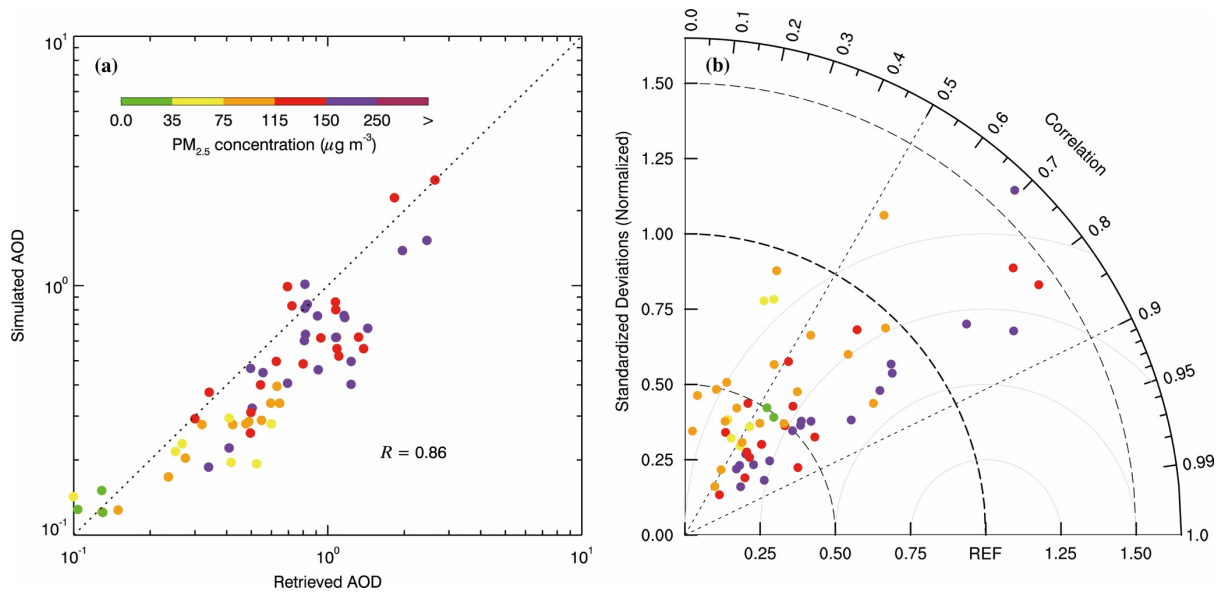
903

904



905  
 906  
 907  
 908  
 909  
 910  
 911  
 912  
 913  
 914  
 915  
 916  
 917

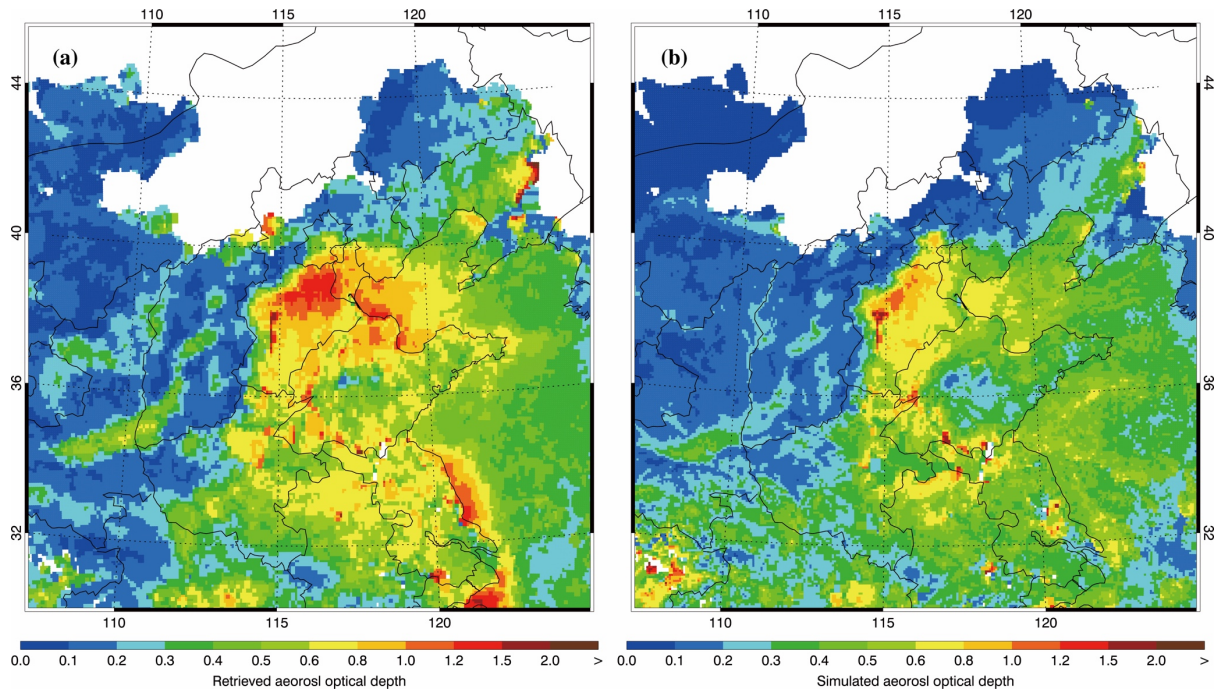
Figure 1 (a) **WRF-Chem** simulation domain with topography and (b) North China Plain. In (a), the blue circles represent centers of cities with ambient monitoring sites in, and the size of blue circles denotes the number of ambient monitoring sites of cities. In (b), the blue and red filled circles denote the NCNST and IRSDE site, respectively, and the red filled rectangle denotes the meteorological site. The red numbers denote the CERN sites with the solar radiation measurement. 1: Beijing urban; 2: Jiaozhouwan; 3: Yucheng; 4: Luancheng.



918  
 919  
 920  
 921  
 922  
 923  
 924  
 925  
 926  
 927

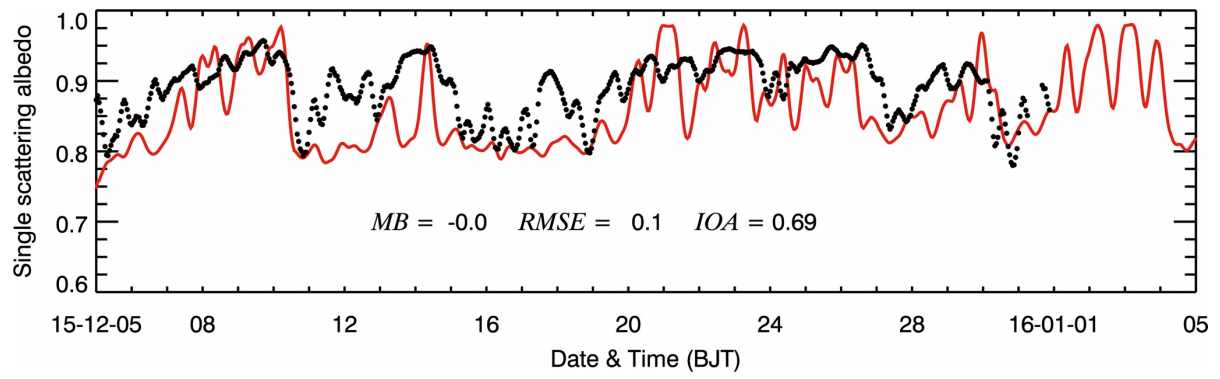
Figure 2 (a) Scatter plot of the MODIS retrieved and simulated daily AOD, (b) Taylor diagram (Taylor, 2001) to present the variance, bias and correlation of the retrieved and simulated daily AOD averaged in the NCP from 05 December 2015 to 04 January 2016.





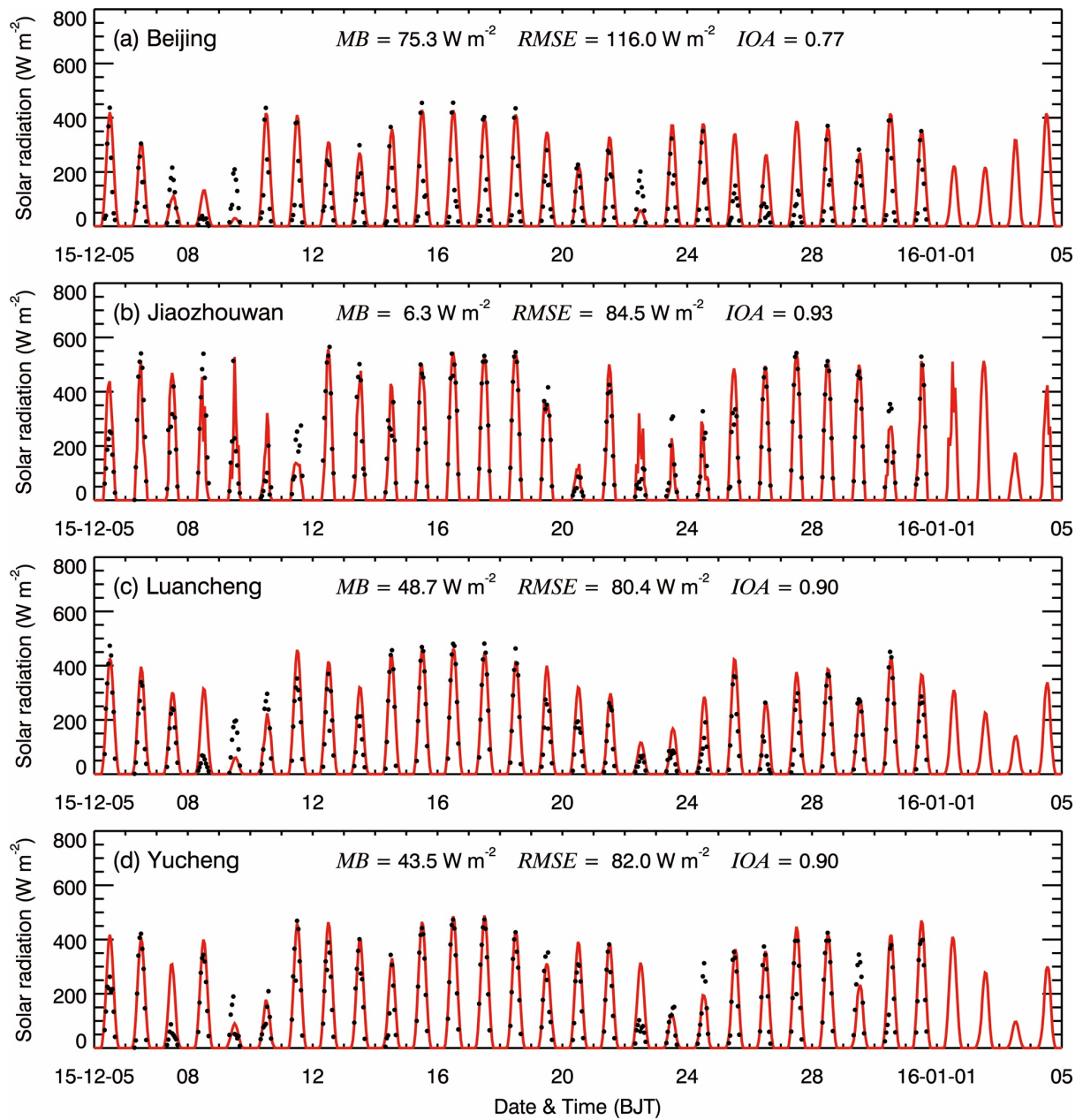
928  
 929  
 930  
 931  
 932  
 933  
 934  
 935  
 936

Figure 3 Spatial distribution of (a) retrieved and (b) simulated AOD averaged from 05 December 2015 to 04 January 2016 in the NCP.



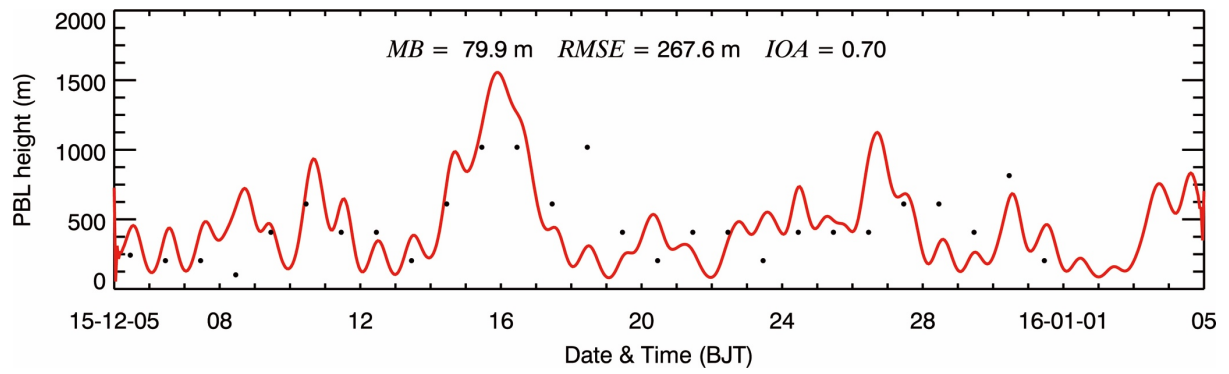
937  
 938  
 939  
 940  
 941  
 942  
 943  
 944  
 945

Figure 4 Comparison of measured (black dots) and predicted (red line) diurnal profiles of SSA in Beijing from 05 December 2015 to 04 January 2016.



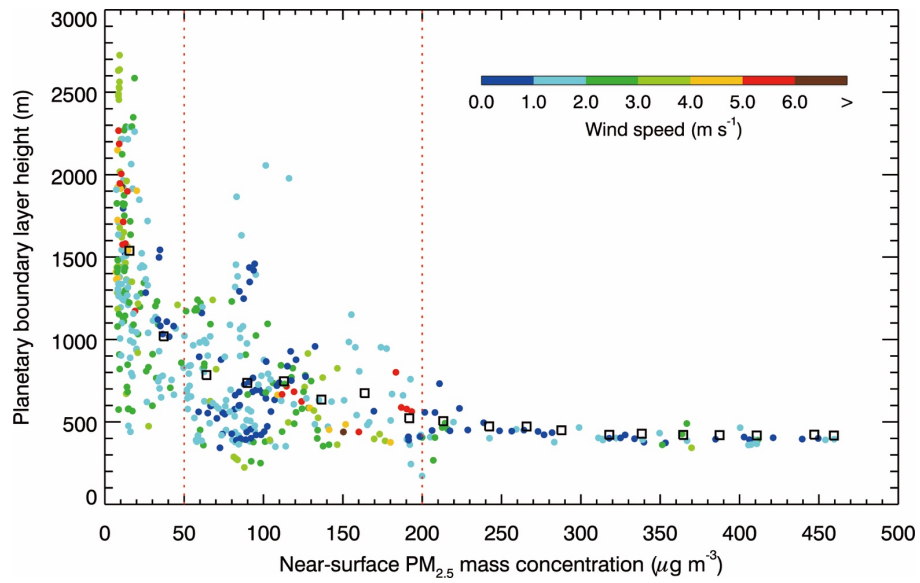
946  
 947  
 948  
 949  
 950  
 951  
 952  
 953  
 954  
 955

Figure 5 Comparison of measured (black dots) and predicted (red line) diurnal profiles of the SWDOWN reaching the ground surface in (a) Beijing, (b) Jiaozhouwan, (c) Luancheng, and (d) Yucheng from 05 December 2015 to 04 January 2016.



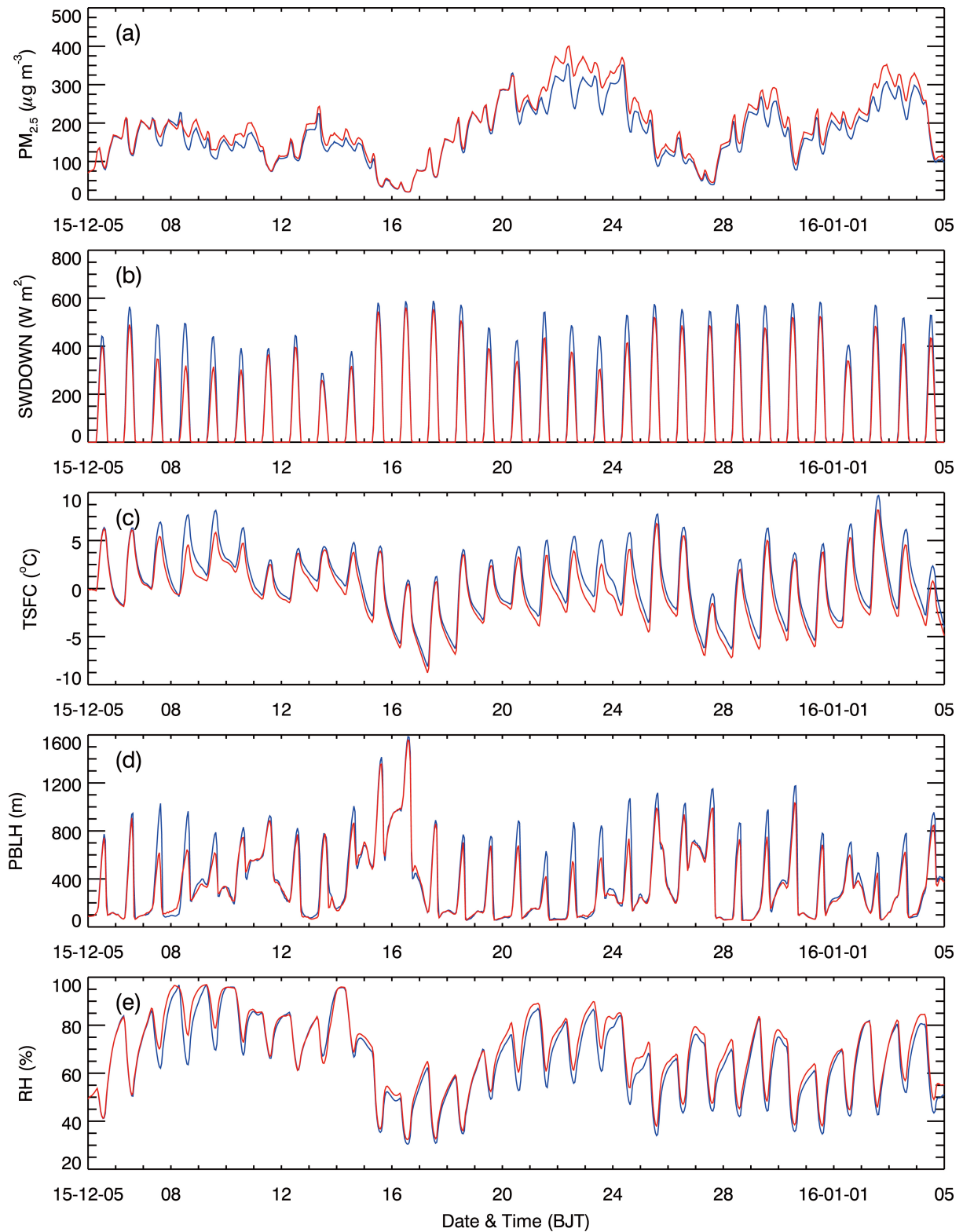
956  
 957  
 958  
 959  
 960  
 961  
 962  
 963  
 964

Figure 6 Comparison of predicted diurnal profile (red line) of PBLH from 05 December 2015 to 04 January 2016 with observations at 12:00 BJT in Beijing.



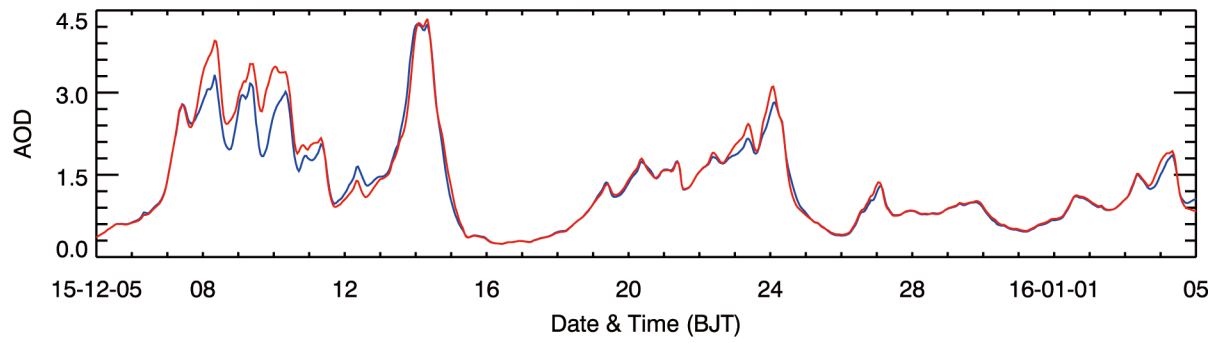
965  
966  
967  
968  
969  
970  
971  
972  
973  
974

Figure 7 Scatter plot of the PBLH and near-surface [PM<sub>2.5</sub>] at IRSDE site from 12 January to 20 February 2014. The black rectangle shows the bin average of PBLH. The color of the filled circles denotes the WSPD at the meteorological site close to IRSDE in Figure 1b.



975  
 976  
 977  
 978  
 979  
 980  
 981  
 982  
 983

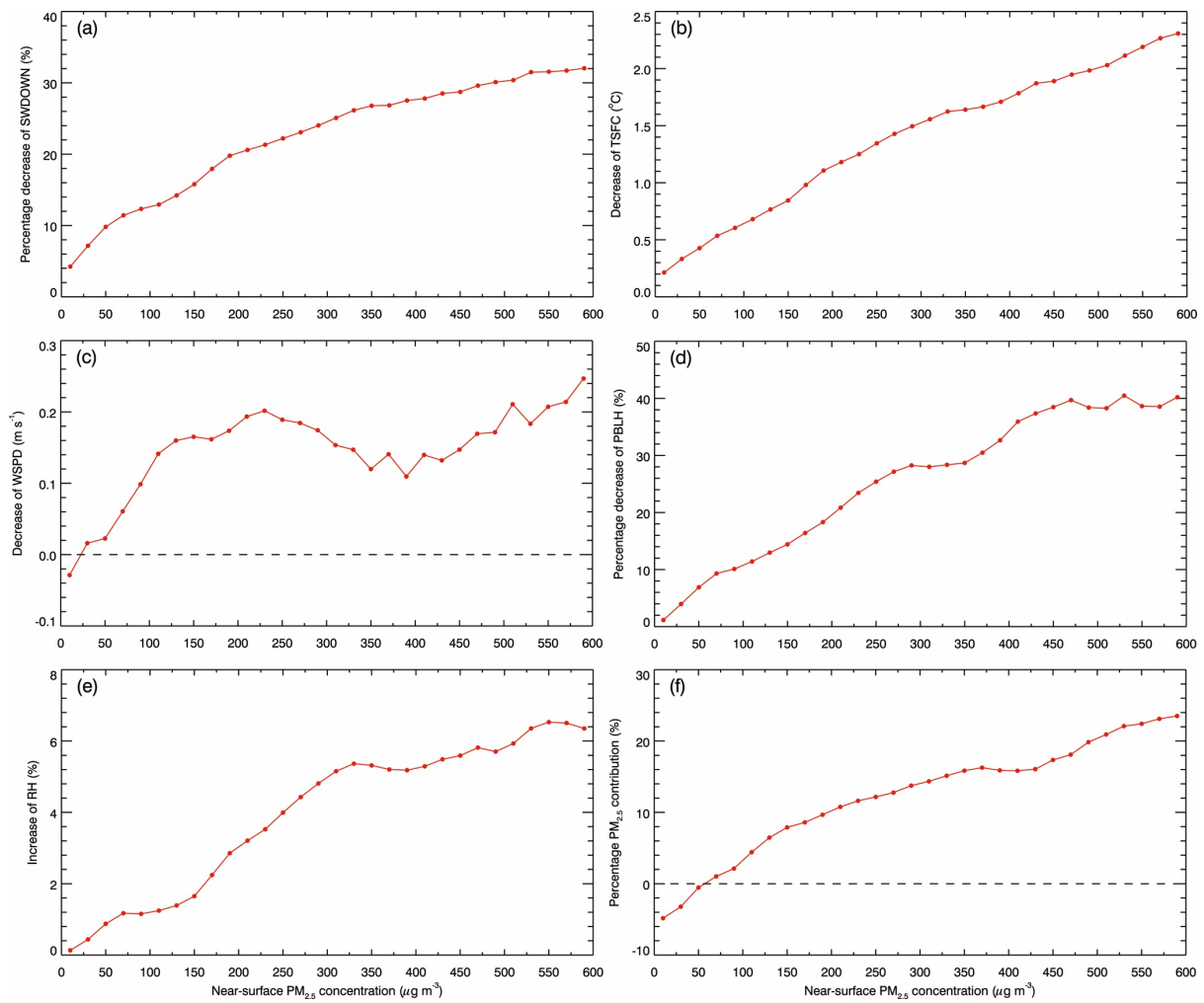
Figure 8 Temporal variations of the average (a) near-surface  $[PM_{2.5}]$ , (b) SWDOWN at the ground surface, (c) TSFC, (d) PBLH, and (e) RH in the most polluted area in the NCP with  $[PM_{2.5}]$  of more than  $150 \mu g m^{-3}$  in  $f_{base}$  (red solid line) and  $f_{rad0}$  (blue solid line) from 05 December 2015 to 04 January 2016.



984  
 985  
 986  
 987  
 988  
 989  
 990  
 991  
 992  
 993

Figure 9 Temporal variations of the average AOD at 550nm in the most polluted area in the NCP with  $[PM_{2.5}]$  of more than  $150 \mu\text{g m}^{-3}$  in  $f_{base}$  (red solid line) and  $f_{rad0}$  (blue solid line) from 05 December 2015 to 04 January 2016.





994

995 Figure 10 Average (a) percentage decrease of SWDOWN at the ground surface, (b) decrease  
 996 of TSFC, (c) decrease of WSPD, (d) percentage decrease of PBLH, (e) increase of RH, and (f)  
 997 percentage contribution of near-surface  $[PM_{2.5}]$  caused by ARF, as a function of the  
 998 near-surface  $[PM_{2.5}]$  in the NCP during daytime from 05 December 2015 to 04 January 2016.

999

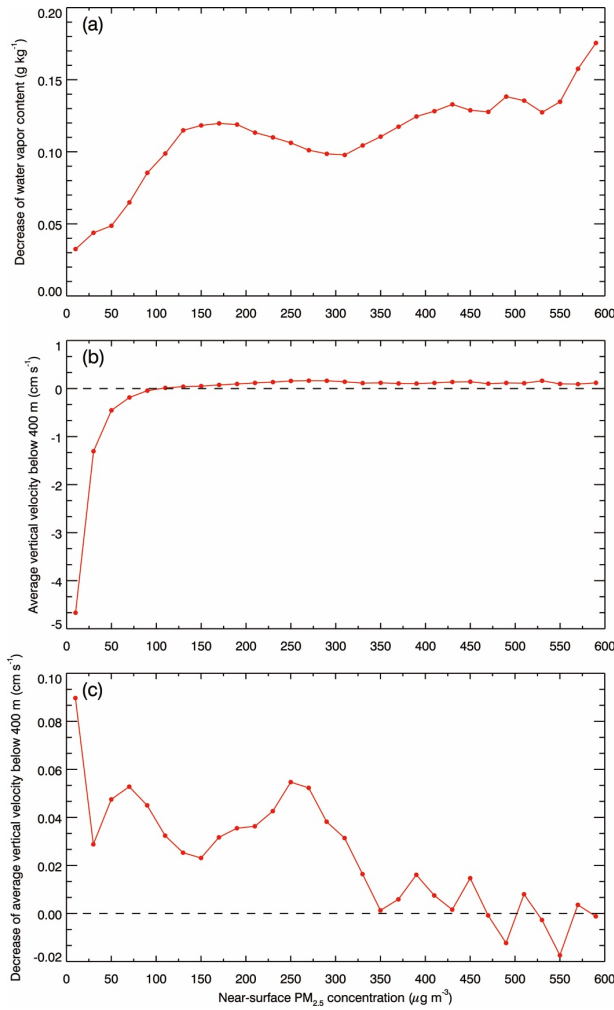
1000

1001

1002

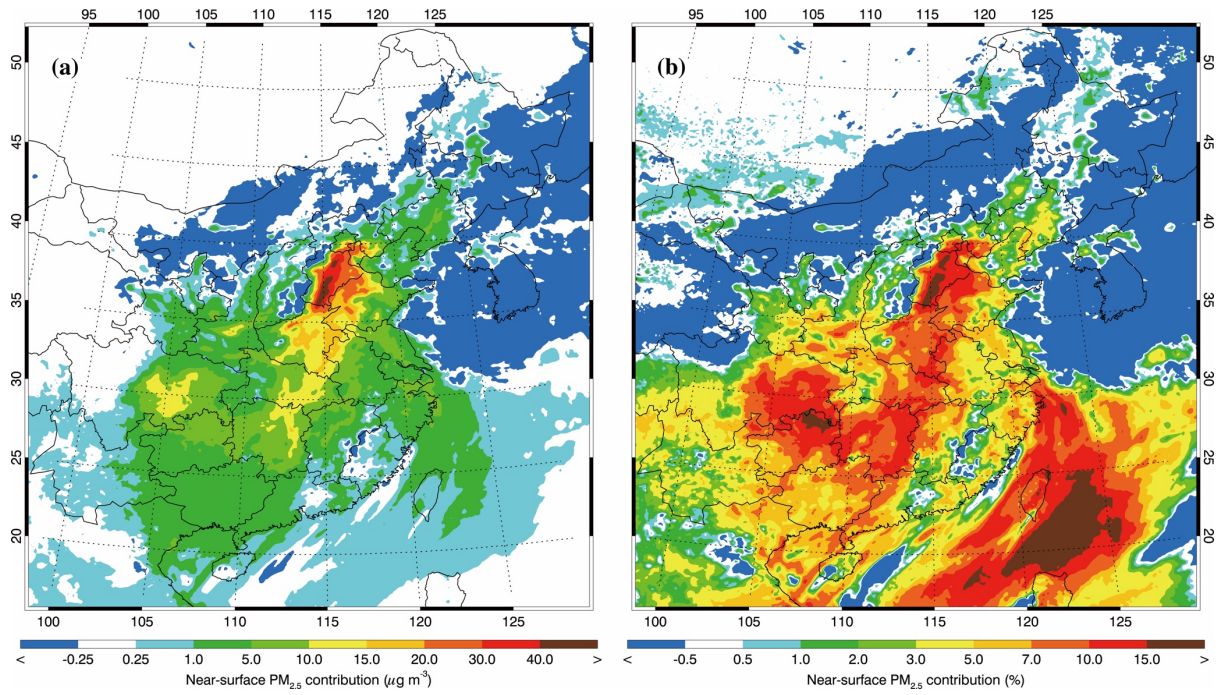
1003





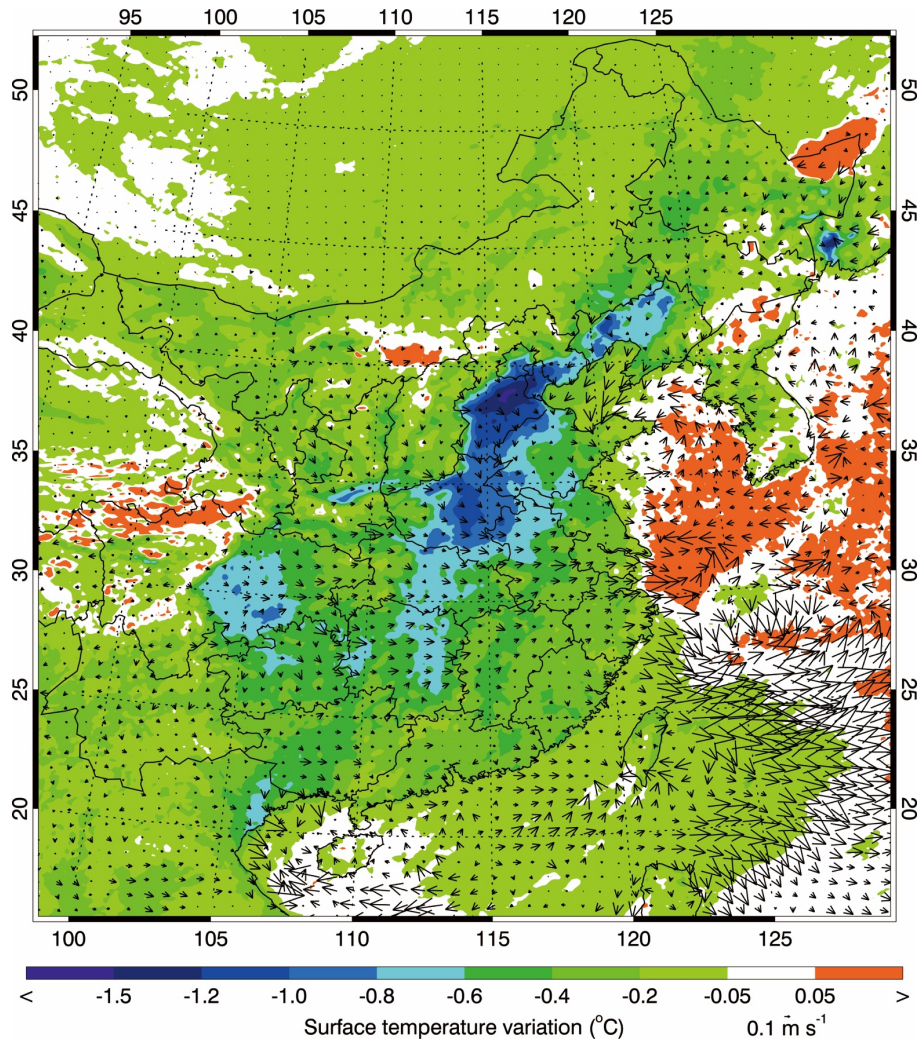
1004  
 1005  
 1006  
 1007  
 1008  
 1009  
 1010  
 1011  
 1012  
 1013  
 1014

Figure 11 Average (a) decrease of water vapor content and (c) decrease of average vertical velocity below 400 m caused by ARF, and (b) average vertical velocity below 400 m in  $f_{rad0}$  as a function of the near-surface [PM<sub>2.5</sub>] in the NCP during daytime from 05 December 2015 to 04 January 2016.



1015  
 1016  
 1017  
 1018  
 1019  
 1020  
 1021  
 1022  
 1023

Figure 12 Near-surface [PM<sub>2.5</sub>] contribution caused by ARF, averaged from 05 December 2015 to 04 January 2016 in the NCP.



1024  
 1025  
 1026  
 1027  
 1028  
 1029  
 1030  
 1031

Figure 13 TSFC and wind field variations caused by ARF, averaged from 05 December 2015 to 04 January 2016 in the NCP.